UNIVERSIDADE D
COIMBRA

José Luís Bento Lago de Queiroz

STUDY OF VOXEL TEMPERATURE DURING 3D DIRECT LASER WRITING

IN-SITU LOCAL TEMPERATURE MEASUREMENT OF PURE AND PHOTOINITIATOR-DOPED SZ2080 PHOTORESIST USING UPCONVERTING NANOCRYSTALS

Dissertação no âmbito do Mestrado Integrado em Engenharia Física, Área de Instrumentação,
orientada pelo Doutor Mangirdas Malinauskas e pelo Professor Doutor Rui César do Espírito Santo Vilão
e apresentada ao Departamento de Física da Faculdade de Ciências e Tecnologias da Universidade de Coimbra.

Setembro de 2019

• Faculdade de Ciências e Tecnologias da Universidade de Coimbra •
Departamento de Física

Study of voxel temperature during 3D direct laser writing

In-situ local temperature measurement of pure and photoinitiator-doped SZ2080 photoresist using Upconverting Nanocrystals.

Thesis made in collaboration with the
Laser Nanophotonics group of the Vilnius University Laser Research Center

by MSc St. José Bento Queiroz

VU Guidance: Dr. Mangirdas Malinauskas
PhD St. Simonas Varapnickas

UC Guidance: Prof. Dr. Rui Vilão

Masters Final Thesis in Physics Engineering:
Area of Instrumentation

Coimbra, 2019

"This evening I play for my friend Vytautas.
We'll play one thing.
It's called 'Vilnius Poker'."

Ričardas Gavelis
Vilnius Poker

Aos meus pais, ao Gui e ao João

Acknowledgements

First of all I would like to thank the whole Laser Nanophotonics group of Vilnius University Laser Research Centre, for receiving me with open arms and guiding me in every step of this work with their knowledge, experience and companionship. In particular I would like to thanks Simonas Varapnickas, for actively watching my steps closer than anyone and for the support he gave me during my time in Lithuania, as well as Dr. Mangirdas and Darius for all the help given along the way. A special thanks goes to my supervisor Professor Rui Vilão, and for his active interest in my work.

I would also like to thank every friend I found during the course of this year, who made this whole experience a remarkable journey. In particular to Mimi and Till, my german family for 6 months.

Quero agradecer a todos os meus amigos que fizeram parte deste meu percurso académico, a todo o Departamento de Física da Universidade de Coimbra e ao CUMN, por me ter ajudado no estudo, na amizade e na oração.

Deixo um profundo agradecimento aos meus pais, que tornaram todo este percurso possível, aos meus irmãos, ao meu avô Tintim e avô Chinho e às minhas avós Cuncá e Nené, por todo o apoio e valores que me passaram e que agoram me levam a passar esta meta.

Por último queria agradecer à Francisca, pela amizade, apoio e todo esforço feito para que caminhássemos sempre juntos, também durante estes anos de curso.

Resumo

3D direct laser writing (3D DLW) é uma técnica de fabricação que cresceu rapidamente nas últimas décadas devido à capacidade que tem de criar estruturas 3D na região dos micrómetros e até mesmo nanómetros, sendo de um grande interesse para diversas áreas de aplicação, como na bioengenharia e fotónica. Apesar de apresentar um futuro promissor, é necessário um estudo aprofundado dos mecanismos por detrás desta técnica de forma a optimizar os materiais e processos utilizados. Nesta dissertação irá ser apresentado um método de medição da variação da temperatura local em amostras de pré-polímero SZ2080 puro e dopado com foto-iniciadores durante o processo de *3D direct laser writing*, recorrendo a *upconverting nanocrystals* (UCNCs) como nano-termómetros ópticos. Para isso foi concebido e desenvolvido um set-up óptico para este estudo, capaz de simultâneamente realizar o processo de direct laser writing e capturar o espectro de fluorescência emitido pelos UCNCs presentes nas amostras de SZ2080. A medição das temperaturas locais foi realizada recorrendo ao cálculo do rácio da intensidade de fluorescência (FIR) usando os espectros capturados provenientes dos UCNCs. O set-up desenvolvido neste estudo executou com êxito as calibrações dos valores de FIR com a temperatura, posteriormente usadas para as medições da temperatura local nas amostras de SZ2080 puras e dopadas com foto-iniciadores durante o processo de *direct laser writing*. As medições realizadas *in-situ* dos valores para as temperaturas locais, utilizando o mesmo set-up, não apresentam nenhum aumento da temperatura tanto para as amostras de SZ2080 puro como para as amostras de SZ2080 dopado com foto-iniciadores.

Key words: Direct Laser Writing, Pré-polímero, Foto-iniciador, Upconverting Nanocrystals, Nanotermómetros

Abstract

3D direct laser writing (3D DLW) is a technique which has grown fast in the last decades and due to the ability of creating fine 3D polymer structures in the micro- and nano- regions it is of great interest for several fields of applications such as in bioengineering and photonics. Even though it presents a promising future, one needs to further understand the underlying mechanics of this technique in order to optimize the materials and processes. In this work we will be presenting a method to measure local temperature differences in photoinitiator (PI) doped and undoped SZ2080 photoresist samples during the process of 3D direct laser writing, using upconversion nanocrystals (UCNCs) as optical nanothermometers. For this an optical set-up was designed and developed in this work for a simultaneous direct laser writing and gathering of upconversion fluorescence spectra emitted by the UCNCs present in the SZ2080 samples. The local temperature measurements were made recurring to fluorescence intensity ratio (FIR) calculations using the captured UCNCs spectra. The set-up built in this work was successfully able to perform FIR temperature calibrations, later used for local temperature measurements on our PI doped and undoped SZ2080 photoresist samples during laser writing. Upon measuring the *in-situ* local temperature values, using the same set-up, no temperature increase was observed for both PI-doped and undoped SZ2080 samples.

Keywords: Direct Laser Writing, Photoresist, Photoinitiator, Upconverting Nanocrystals, Nanothermometry

List of Figures

List of Tables

Contents

Chapter 1

Introduction

1.1 The uprising of 3D Nano-fabrication

Today's technological world reaches a stand where volume becomes an important issue for components and mechanisms. If some system can be reduced in its dimensions while maintaining their workability, not only they should but sooner or later they will. From the electronics world to the mechanical engineering field, one can hardly miss cases of this technological "*Drink me* potion" [1] during the last decades.

This need for smaller and more powerful systems creates the urgency for developing and improving fabrication methods. Electron-beam lithography (mainly used in the microchip industry) and Molecular beam epitaxy (MBE) are two big examples of techniques developed in the last five decades that enable structure designs with increasingly small features (<10nm for electron-beam lithography, while for the MBE layering process, even atomic precision can be reached). Even though most of these state of the art techniques present very high precisions, they are restricted to 2D structures development, and it was not until the end of the last century (1997) that one technique for 2.5D and 3D photo-polymerization micro-structuring was presented - 3D Direct Laser Writing or 3D DLW.

3D Direct Laser Writing (3D DLW), as the name implies, allows the micro-/nano-fabrication

[1] The infamous shrinking potion drank by Alice in Lewis Carroll's classic *Alice in Wonderland*.

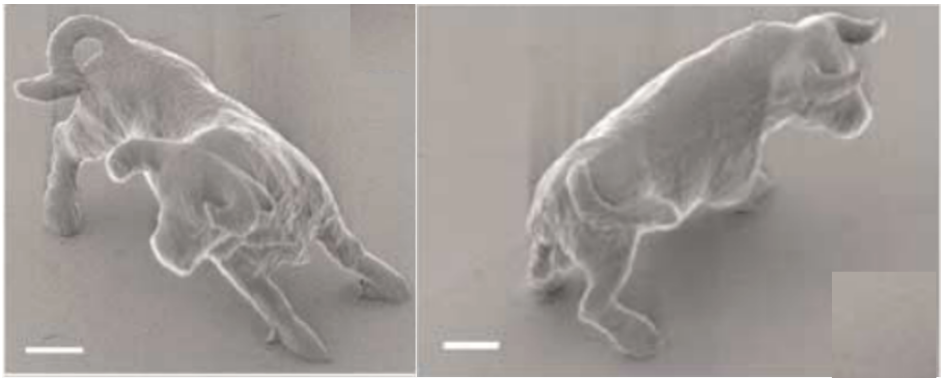

Figure 1.1.1 – Sculpture of a micro-bull built with 3D DLW. Considered to be the smallest animal sculpture ever fabricated. Scale bar is 2 μm. Extracted from [Kawata et al., 2001].

of 3D polymer structures recurring to tightly focussed infra-red laser sources. Thanks to the maturation of this process in the past decade, including the study of new, more suitable, pre-polymer materials as well as optimized optics, the current finest feature size is in the order of 100 nm [Malinauskas et al., 2010]. In figure 1.1.1 one can see an example of a sculpture of a bull built using this technique by Kawate *et al.*. This "micro-bull", as named in the original paper [Kawata et al., 2001], is about the size of a red blood cell (10 μm x 7 μm) and was produced with a fabrication accuracy of ~150 nm.

The current applications for 3D DLW are mainly focused in photonic devices and in the micromachinery area, although some bioengineering applications are starting to arise. In photonic devices it is easy to understand the potential of this technique, since it can create optic elements in a very small scale, taking advantage of the refractive index of the built polymer and the easy manipulation of the general structure of the elements.

In figure 1.1.2 one can see electron-microscope images of three important micro-optical structures built with 3D direct laser writing: waveguides and couplers, gratings and zone plates, and photonic crystals. More information about the building mechanism and workability of these structures can be found elsewhere [Žukauskas et al., 2016].

In the micromachinery realm, some simple working mechanisms were developed in the last decades, but they still haven't found a place in a particular real-world application. However, they demonstrate the ability of creating movable gears, springs and other different me-

chanical components which are essential elements for possible future designs of more complex structures. Some of these micromachines can be seen in figure 1.1.3.

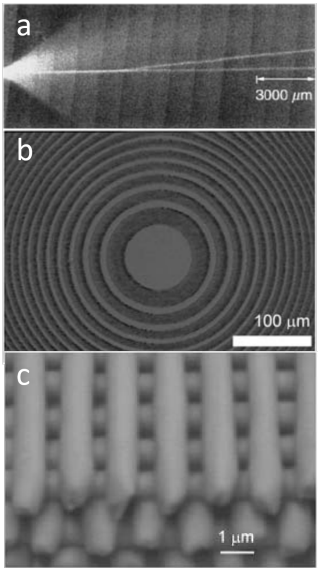

Figure 1.1.2 – SEM images of three micro-optical elements fabricated through 3D DLW. **(a)** Wave coupler drawn in pure silica. Light follows through the Y shaped coupler with little attenuation. **(b)** Fresnel zone plate. **(c)** Woodpile structure, an example of a photonic crystal (PhC). Extracted from [Sun and Kawata, 2004].

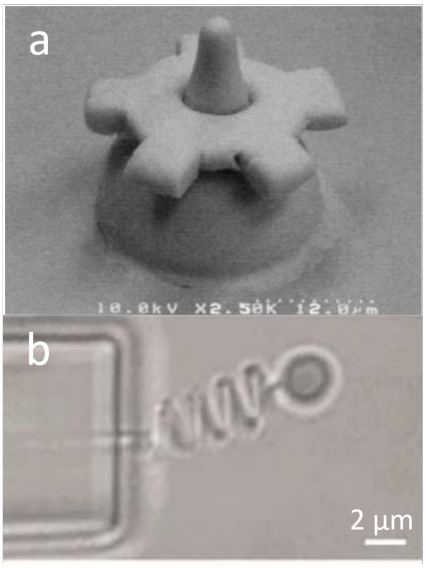

Figure 1.1.3 – SEM images of two micro-mechanical elements fabricated through 3D DLW. **(a)** A rotating gear on a still shaft. Extracted from [Sun and Kawata, 2004] **(b)** A functional polymer spring and ball attached to a immobile polymer block. Extracted from [Kawata et al., 2001].

About the bioengineering applications, even though they are still in an early stage, some positive results already arose. One example of this usage is the nano-fabrication of polymer scaffolds to serve as a structural support in tissue growth processes [Danilevičius et al., 2013, Malinauskas et al., 2016].

Even though 3D DLW applications are promising, they rely on the continuous studying of this technique. Important steps are yet to be done in order for 3D DLW to achieve a point of industrial feasibility, such as the development of better and optimized materials for each application as well as a precise and functional method for fast structuring which, ideally, can be scaled to build several structures simultaneously. Almost all of these steps, specially the

development of new materials, require a deep understanding of the mechanisms underlying 3D DLW and how can they be manipulated in one's advantage. In this dissertation, the temperature effects during the writing process will fall under the scope (not only figuratively), introducing a set-up for studying the *In-situ* local temperature of the material.

1.2 3D Direct Laser Writing Nano-Lithography

Photopolymerization is the widely used concept upon which 3D Direct Laser Writing (3D DLW) technology bases itself. By irradiating light with a specific wavelength (usually in the ultra-violet region) on a selected material (a pre-polymer or photoresists), one can, through photo-chemical processes, polymerize the material, changing its intrinsic characteristics. These pre-polymers, or photoresists can be mainly separated into two groups for this approach: positive-tone and negative-tone photoresists, depending on whether they become respectively more or less soluble in a given solvent after irradiation. The solubility of the material is crucial in the process of developing the sample, which is done by dipping it in a solvent, leaving only the intended part of the material (the non-soluble part).

In these "traditional" photoplolymerization methods, the photoresists used are developed in a way where their absorption spectra is optimized for the light used in the curing process. This means that if you expose a layer of these photoresists with the intended light-source, the main intensity of the incident light will be absorbed by the surface and near-surface layers of the material, polymerizing the sample only to a certain depth. The depth of this polymerization can still vary depending on the intensity of the source and the characteristics of the material, but the process is always limited by this factor. More complex structures built with this technique have to be written layer by layer, by depositing the photoresist, polymerizing and developing it for every layer. This turns it into a very time-consuming process.

One area where this type of photopolymerization process is widely used is in the silicon wafer optical lithography process, as seen in [Mack, 2007], since the required structures do

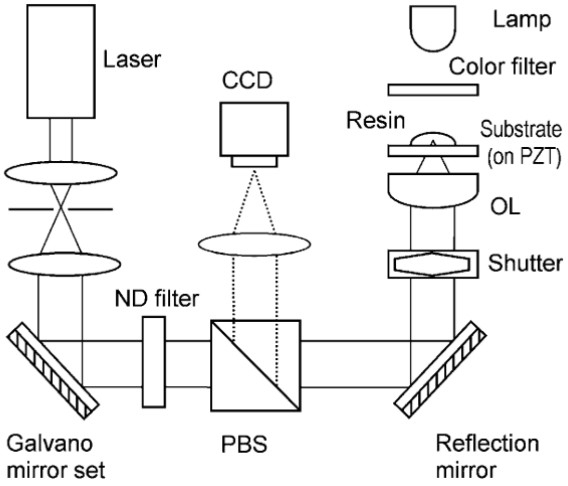

Figure 1.2.1 – General set-up scheme for 3D DLW using Two Photon Polymerization (TPP). A Laser beam, after manipulation, is focussed in the resin (photoresist) through an Objective Lens (OL). A Galvano mirror set is an electric controlled mirror for precise laser alignments. A neutral density filter (ND filter) can be used to reduce the laser beam power. The polarized beam splitter (PBS) is important to separate the laser beam from the backlighting image redirected to the CCD camera. The shutter is used to control laser exposition on the sample and PZT refers to the piezoelectric scanning stage. The Lamp and CCD are used for *in-situ* imaging. Extracted from [Sun and Kawata, 2004].

not present high complexity.

Several approaches were developed to optimize the fabrication of 3D photo-polymerized structures [Sun and Kawata, 2004], but in this work only 3D Direct Laser Writing through multi-photon polymerization will be discussed. This method, compared to other solutions, requires a simpler set-up, being preferred by several groups that work in this field.

The process of 3D Direct Laser Writing bypasses surface absorption of normal photoresists, being able to polymerize voxels [2] inside the photoresist sample, without polymerizing any other part of the material. This enables the fabrication of complex structures, voxel by voxel, in a similar way to the now common commercial 3D printers.

Figure 1.2.1 presents a scheme of a 3D Direct Laser Writing through multi-photon polymerization. The two main components of that set-up that enable the photo-polymerization

[2] Small ellipsoid polymerized volumes originated in the focal volume of the writing laser when focussed inside a photoresist.

to occur are the Laser and the objective lens (OL), through which the laser beam is focussed in the photoresist (Resin). To better understand this process it will be presented step by step, through its three main concepts: the ***Multi-photon absorption***, the importance of using ***Femtosecond pulsed lasers*** and the ***Photo-polymerization process*** at a molecular level.

• Multi-Photon Absorption

3D Direct Laser Writing, even though it uses the same materials used in the "traditional" photopolymerization approach, is able to produce *in-depth* structures in the photoresist using a trick up the sleeve. This trick comes by the hand of Maria Goeppert-Mayer, who predicted the mechanism of multi-photon absorption on her doctoral thesis, back in 1931.

Multi-photon absorption is a non-linear optical process in which two or more low-energy photons ($E_{\gamma 1}$...$E_{\gamma n}$), not necessarily with the same energy, are absorbed by a molecule in a way that it creates the same effect as the absorption of a photon with an energy equal to the sum of the energy of the low-energy photons absorbed ($E_{\gamma}^{final} = E_{\gamma 1}$+...+$E_{\gamma n}$).

Maria Goeppert-Mayer's theory predicts that this still holds even if the absorbing molecule has no intermediary excited states between the initial energy state (E_0) and the final energy state ($E_0 + E_{\gamma}^{final}$), meaning that the molecule can be transparent considering linear absorption of the low-energy photons but not if it absorbs a set that, together, have the energy needed to excite the absorbing molecule. However, for this effect to take place, the low-energy photons need to be absorbed "simultaneously", implying that it happens in a period of time of the order of some femtoseconds, taking into consideration Heisenberg's Uncertainty Principle.

The very short period of time between absorptions is considered to be the lifetime of a *virtual* excited state for which the first low-level photon excites the molecule, and from which the subsequent photons will excite the molecule to another *virtual state* or to the final energy state. The example of simultaneous two-photon absorption (TPA, the main example of multi-photon absorption) and the formation of this *virtual state* is depicted in figure 1.2.2.

It becomes obvious that for this effect to take place, due to the short period of time re-

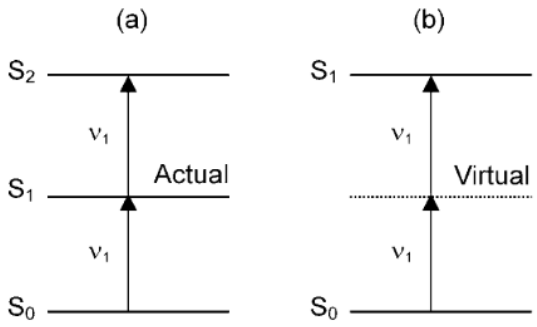

Figure 1.2.2 – Scheme of degenerate two-photon absorptions (TPA) **(a)** TPA *via* an actual state **(b)** simultaneous TPA with the creation of a virtual state. Extracted from [Sun and Kawata, 2004].

quired between photon absorption, the intensity of the photon beam needs to be relatively high. For this, it is needed to introduce another factor of extremely importance to this process: the use of femtosecond pulsed lasers.

Although this is a fundamental concept for the understanding of 3D DLW, it is important to note that it is not the only mechanism behind this technique. Others, like electron avalanche effects, are extremely relevant and can even produce higher rates of electrons than multi-photon absorption [Malinauskas et al., 2010]. This is further explained below in ***Polymerization Processes***.

• **Femtosecond Pulsed Lasers**

The femtosecond pulsed lasers have two main advantages that, together, combine the necessary conditions for the development of this technique: the extremely short pulse duration and the beam wavelength.

Ultra-short pulses produced by these type of lasers (in the order of 100-300fs) increase substantially the amount of power per pulse delivered to the sample, and thus, the photon intensity. This higher photon intensity is fundamental for the non-linear optical effects to take place, since the probability of occurrence of non-linear effects increases with increasing intensity (e.g. for degenerate TPA, the cross section equation grows with I^2 [Sun and Kawata, 2004]), and to overcome the threshold intensity needed for polymerization to take place.

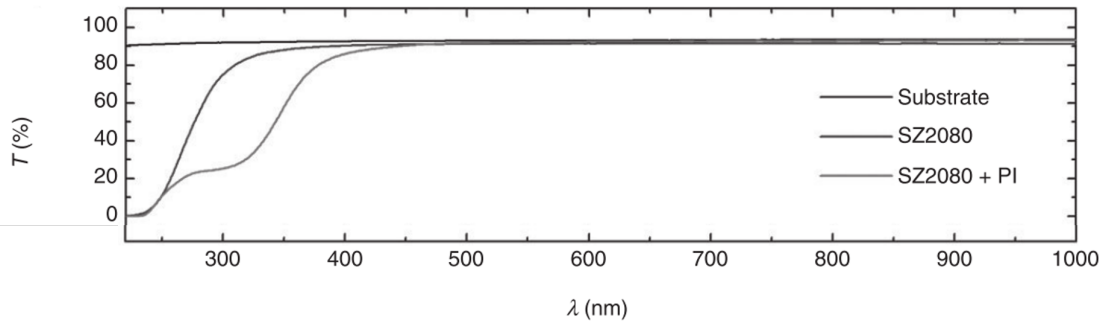

Figure 1.2.3 – Example of a transmittance spectra of a photoresist, in this case SZ2080, pure and doped with photoinitiator (PI)). Extracted from [Žukauskas et al., 2016].

The short time duration of the pulses has also a main role in the heating processes of the sample. Considering that the pulse energy deposition is faster than the average energy dissipation in the materials lattice (electron-lattice transfer or phonon emission), the excitation turns to be heat insulating for the duration of the pulse, accumulating heat inside the focal volume. This thermal effect can influence the writing resolution thanks to a secondary heat-induced photo-polymerization [Fischer et al., 2013]. Further accumulation or dissipation of heat in that restricted volume is dependent on laser repetition rate.

Another important factor is the laser wavelength. Common femtosecond lasers have a beam wavelength that falls in the near infra-red (NIR) region, most photoresists have a high transmission rate in the region 700 - 1000 nm (see an exaple in figure 1.2.3). The transparency of the material to the laser beam means that no linear-absorption takes place, only high order ones, and even these only occur in the presence of a threshold photon intensity. This makes *in-depth* focussing of the laser possible.

By focussing a femtosecond laser beam onto the sample, using a microscope objective, one can create the necessary conditions for polymerizing a constrained volume inside the photoresist (a *voxel*). Adjusting the delivered power of the laser and considering that the laser will not be absorbed by the material, the threshold intensity for multi-photon absorption will only happen in the focal volume. The dimension of the focal volume can be decreased or increased by choosing an objective with a higher or smaller value of numerical aperture

(NA), respectively, and with that the size of the polarized voxel. High order NA objectives are then used to produce more precise structures with smaller features.

• **Polymerization process**

The polymerization process, common to all photo-polymerization methods using negative-tone photoresists (materials that turn less soluble after exposure), can be separated into three main steps: initiation, propagation and termination.

During the initiation step, photoinitiators - PI - absorb photons depending on the mechanism behind the main absorption effect of the process. In the example of 3D DLW using two photon polymerization, multi-photon effects are the ones present (TPA being the most probable). After photon absorption photoinitiators turn into primary radicals - $PI^{\bullet}$ - that add to monomer molecules - M, turning these into reactive elements able to link to other monomer molecules - $M^{\bullet}$. The two main initiation reaction are described in reactions 1.1 and 1.2.

$$\text{Initiation:} \qquad PI \xrightarrow{TPA} PI^{\bullet} \tag{1.1}$$

$$PI^{\bullet} + M \longrightarrow M^{\bullet} \tag{1.2}$$

$$(M \longrightarrow M^{\bullet}) \tag{1.3}$$

This initiation process is not totally dependent on the presence of photoinitiators in the sample and macro-radicals can sometimes be created directly in the material (reaction 1.3). The mechanism behind reaction 1.3 is mainly associated with the combined effects of the dielectric breakdown of the material (due to high electromagnetic fields present in the focal volume) and the following impact ionization of molecules, due to the acceleration of generated free electrons [Malinauskas et al., 2010]. The low cross-section values for multi-photon absorption of pure photoresists (undoped with photoinitiators) means TPA and other higher-order processes can be neglected, while avalanche ionization becomes dominant.

Even though both mechanisms have the same impact in terms of initiating the polymerization chain reaction, multi-photon absorption has a much lower influence in the local temperature increase inside the focal volume, which protects the material from undesired effects such as thermal expansion or even burning. In order to increase the weight of the TPA mechanism in the initiation process, photoinitiators are used. An example of these initiation reactions for the SZ2080 photoresist (the photoresist used in this work) can be seen in 1.2.4 as well as the molecular structure of the components involved .

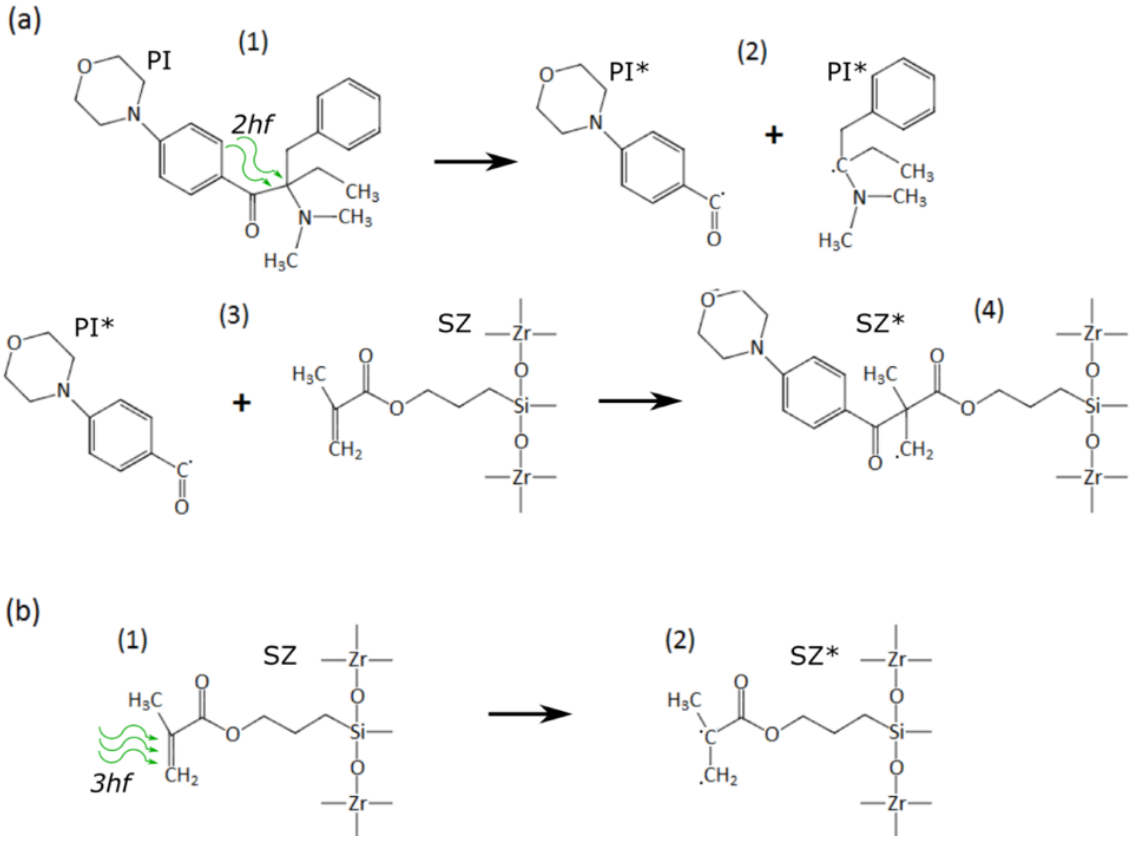

Figure 1.2.4 – **(a)** polymerization reactions initiated by nonlinear absorption of PI molecules and subsequent chemical pathways resulting in a cross linked SZ2080; **(b)** SZ2080 cross linking without PI. hf is the photon energy. Exctracted from [Jonušauskas et al., 2017].

These photoinitiators[3] are molecules specially engineered to have larger TPA cross-sections

[3] In reality, photo-initiator is a general term for a molecule that increases the interaction between the photon and the material (mainly used for applications using linear optical effects), creating reactive species when exposed to radiation. In this work, for the particular case of non-linear optical effects (multi-photon absorption), this general term is used to describe a specific type of photoinitiators that is optimized for this purpose.

at a selected wavelength, which optimizes the laser-material interaction in terms of non-linear optical effects, lowering the threshold power for writing [Sun and Kawata, 2004].

After the creation of monomer radicals - $M^{\bullet}$ - follows the creation and propagation of a chain of monomers that are aggregated to this initial radical (reaction 1.4) or to already linked monomers (reaction 1.5). This creates a macro-radical with n linked monomers -$\tilde{M}_n^{\bullet}$.

$$\text{Propagation:} \qquad M^{\bullet} + M \longrightarrow \tilde{M}_2^{\bullet} \tag{1.4}$$

$$\tilde{M}_n^{\bullet} + M \longrightarrow \tilde{M}_{n+1}^{\bullet} \tag{1.5}$$

For this chain growth to stop and to turn the macro-radical into a polymer chain, some termination processes must be present. The primary termination happens when a macro-radical links to a photo-initiator radical (reaction 1.6), and it is of major importance when working with high photo-initiator concentrations or high photon intensity. There is also the bimolecular termination, when two macro-radical mutually react (reaction 1.7), resulting in a polymer chain with the dimension of the joint macro-radicals.

Primary and bimolecular terminations are the main processes stopping the chain reaction but others do it as well, like the monomolecular termination - where a macro-radical ends up "trapped" by polymerized material (reaction 1.8), or chain transfer - where macro-radicals react with impurities in the photoresist (reaction 1.9).

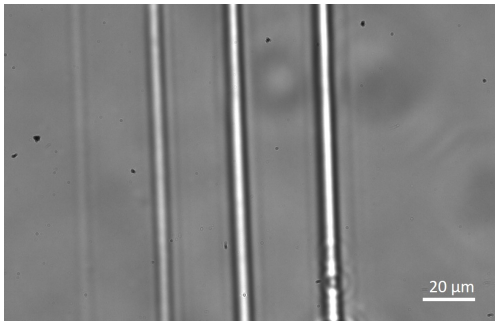

Figure 1.2.5 – Image of polymerized lines using a CMOS camera during the writing process. The polymerized material is easily distinguished due to a refractive index change, making it brighter in the image.

Termination: $\tilde{M}_n^{\bullet} + PI^{\bullet} \longrightarrow$ Polymer chain (primary) (1.6)

$\tilde{M}_n^{\bullet} + \tilde{M}_n^{\bullet} \longrightarrow$ Polymer chain (bimolecular) (1.7)

(other processes:)

$\tilde{M}_n^{\bullet} \longrightarrow (M_n^{\bullet})_{\text{trapped}}$ (monomolecular) (1.8)

$\tilde{M}_n^{\bullet} + RH \longrightarrow \tilde{M}_n^{\bullet} H + R^{\bullet}$ (chain transfer) (1.9)

Even though this is a simplified model, it allows the understanding of the overall process, serving the purpose of this work. Other elements are important for a further study of the polymerization process, like cross-linking systems, which can be found elsewhere [Jiang et al., 2014].

After polymerization the material not only becomes less soluble, but it also becomes stiffer than its non-polymerized counterpart and its refractive index (n) also changes ($\Delta n = n_{unpoly} - n_{poly} = \sim 10^{-2}$] for SZ2080 photoresists) [Malinauskas et al., 2010, Žukauskas et al., 2015]. This change enables one to optically track the writing process on the spot (*in-situ*). As seen in figure 1.2.5, an image captured during 3D DLW using a CMOS camera, the already polymerized resin is easily distinguishable.

Whereas the presented model and theory behind 3D DLW is the one that most accurately

predicts the effects of photo-polymerization, some specific points are not yet fully understood and require further investigation (for example, the polymerization mechanics dependency on pulse duration, pulse repetition rate, and polarisation of the writing laser). The key to unravel these and other effects might be the understanding of the importance of heat accumulation and temperature kinetics inside the *voxel*. This statement arises from published work which proposes methods for local *in-situ* temperature measurement with a resolution smaller than the *voxel* size [Mueller et al., 2013, Varapnickas et al., 2018].

These techniques of *voxel* temperature measurements during 3D DLW will be used in this work to study two types of sample: doped (with photoinitiators) and undoped (or pure) photoresists, for results comparison. This was made in order to partially understand the influence of each initiation process of polymerization (TPA, in reaction 1.1 and dielectric breakdown/impact ionization, reaction 1.3) for each of the studied samples. Considering that avalanche ionization is responsible for a larger increase in local temperature increase than two photon absorption (or any multi-photon absorption), and taking into account the fact that it is more present in the processing of undoped material than in doped one, the expected result is to have a greater local *in-situ* temperature increase while processing pure (undoped) photoresists than its doped counterpart. The exact temperature difference is hard to predict theoretically, since the relevance of each of these two mechanisms is not obvious for doped photoresists. Furthermore, it might also help to understand if heat induced polymerization contributes for the general process, which happens if the prepolymer is exposed to temperatures above 150^{o}C [Malinauskas et al., 2010].

1.2.1 *In-situ* local temperature measurements using Upconverting Nanocrystals

In order to understand the thermal effects inside the *voxel* during 3D DLW one needs a way to measure temperature on a scale smaller than the *voxel* dimensions, and ideally at a molecular level. This imposes the use of temperature sensors with a nanometer spatial res-

olution that will not influence nor be influenced by the polymerization process itself. Inside the wide variety of the already existing *nanothermometers* [Jaque and Vetrone, 2012], we will be focussing on the use of upconverting nanocrystals (UCNCs).

Upconverting Nanocrystals are materials doped with rare-earth ions which have a temperature dependent fluorescence spectra, including them in the group of luminescent nanothermometers, working as optical sensors. The great advantages of using upconverting nanocrystals are the small particle size (~10 nm) and the fast pumping and fluorescence de-excitation process, which enable both high spatial and temporal resolutions. Thanks to these attributes, UCNCs have been thoroughly studied as strong applicants for temperature measurements in a small scale, e.g. to study thermal effects inside living cells [Vetrone et al., 2010].

To explain the process of upconversion and how it can be temperature-sensitive, we will study the example of $NaGdF_4$ doped with Er^{3+}, Yb^{3+}, the main nanocrystals used in this work. The choice of using $NaGdF_4$:Er^{3+},Yb^{3+} nanocrystals is the fluorescence spectra intensity (high enough to be detected even with low pumping power), as well as for their largest known variations of spectra intensity with varying temperature for all studied UCNCs. Large spectra variations give higher measurement resolution, an important factor for this work.

The upconversion mechanism is defined as a molecular absorption of two or more photons of lower energies (*pumping*), exciting the molecule, and a subsequent de-excitation of the molecule, releasing a high-energy photon. Similarly to TPA, the energy of the released photon is the sum of energies of the absorbed photons, but even though it does require a relative high intensity of pumping radiation, it does not need a "simultaneous" absorption of photons (as in TPA). In summary, upconversion is a way of transforming low energy photons into high order ones through molecular excitation and de-excitation mechanisms.

In the specific case of $NaGdF_4$:Er^{3+},Yb^{3+}, the pumping radiation used is usually a 920-980 nm light source, which first excites the state Yb^{3+}: $^2F_{7/2}$ electrons ions to the intermediate state of Yb^{3+}: $^2F_{5/2}$. The excited state Yb^{3+}: $^2F_{5/2}$ resonates with the Er^{3+}: $^4I_{15/2}$, enabling

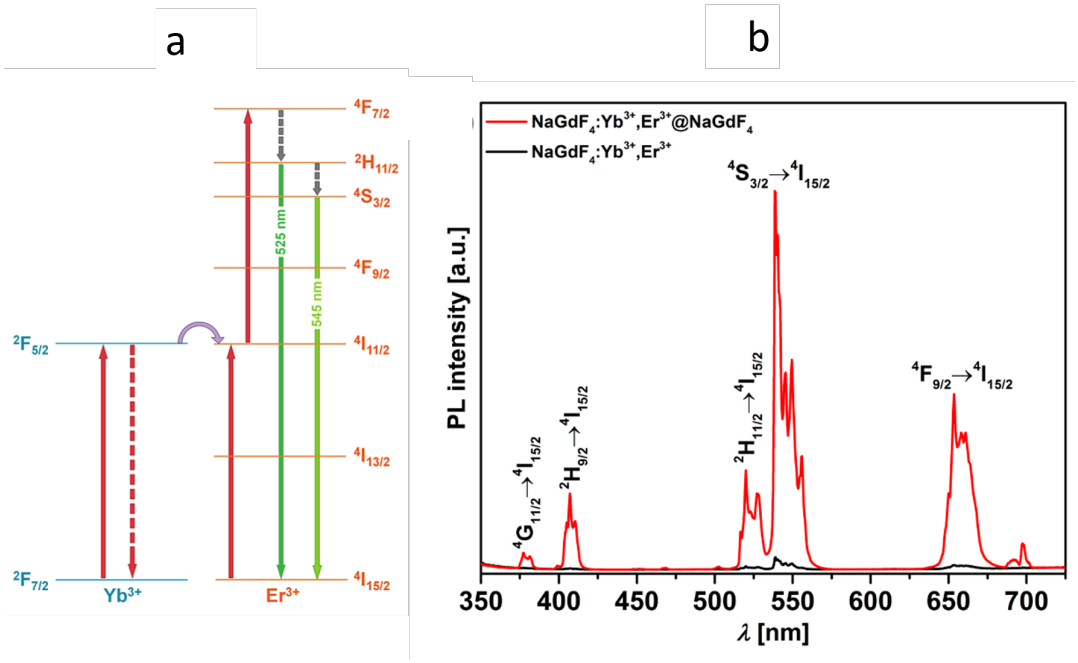

Figure 1.2.6 – **(a)** Simplified level scheme for the upconversion of $NaGdF_4$:Er^{3+},Yb^{3+}. Solid and doted lines represent radiative and non-radiative transitions, respectively. Extracted from [Vetrone et al., 2010] **(b)** Upconversion spectra of $NaGdF_4$:Er^{3+},Yb^{3+}. @NaGdF means nanocrystals in which only the core is doped with Er^3+ and Yb^3+, shielded by a shell of NaGdF. The result of this exterior shell is an improved general luminescence. The initial energy levels for high order transitions depicted in **b** are not present in the energy level diagram **a** since they are of no interest to this work. Extracted from [Varapnickas et al., 2018].

these initially excited electrons to be pumped once more to the $^4F_{7/2}$ level of Er^{3+}. While on this energy level, the excited electrons can suffer non-radiative transitions to the levels of Er^{3+}: $^2H_{11/2}$ and Er^{3+}: $^4S_{3/2}$, from each of these two states they transition to the ground state Er^{3+}: $^4I_{15/2}$, releasing through these transitions 525 nm and 545 nm photons, respectively. These two transitions, (Er^{3+}: $^2H_{11/2}\rightarrow{}^4I_{15/2}$) and ($Er^{3+}$: $^4S_{3/2}\rightarrow{}^4I_{15/2}$), result in a fluorescence spectra consisting of two main peaks in the green region, one between 515 and 525 nm (centred at 525 nm) and the other between 535 and 565 nm (centred at 545 nm). In figure 1.2.6 one can see a simplified energy level scheme for the upconversion process of $NaGdF_4$:Er^{3+},Yb^{3+} as well as the expected fluorescence spectra.

Other transitions are also present, e.g. the non-radiative transition (Er^{3+}: $^4S_{3/2}\rightarrow{}^4F_{9/2}$) followed by the radiative transition (Er^{3+}: $^4F_{9/2}\rightarrow{}^4I_{15/2}$), releasing a photon with a wave-

length of 650 nm. The resulting peaks from these other transitions can be also seen in figure 1.2.6 but it is of no particular interest to this work.

The upconverting property of $NaGdF_4$:Er^{3+},Yb^{3+} comes from the presence of Er^{3+} ions. As seen in figure 1.2.6, the transition (Er^{3+}: $^4I_{15/2} \rightarrow ^4F_{7/2}$) can also happen, making the Er^{3+} ions self sufficient upconverters. The reason to dope the material with Yb^{3+} is its extinction coefficient, which may be low considering most fluorophores and organic dyes, but is 10 times larger than that for Er^{3+}, optimizing the absorption of light. Yb^{3+} is also an efficient sensitizer since it has only one excited state ($^2F_{5/2}$).

The $NaGdF_4$ host matrix has an important role in the upconverting process, as the low-energy phonon spectrum of fluoride-based crystals will not deactivate the luminescence and, in the particular case of $NaGdF_4$, it actually increases luminescence efficiency.

Fluorescence spectra temperature sensitivity of $NaGdF_4$:Er^{3+},Yb^{3+} nano-crystals comes from a thermal influence on the populations distribution on the levels Er^{3+}: $^2H_{11/2}$ and Er^{3+}: $^4S_{3/2}$. With increasing temperature, the rate of $^4S_{3/2}$ non-radiative relaxations increases, but this loss is compensated by a thermalization of populations with the closely spaced level $^2H_{11/2}$. This maintains the population of level $^4S_{3/2}$ more or less constant with varying temperature. The effect it has on the fluorescence spectra is an intensity increase on the 525 nm centred peak (as normally expected for every peak) and an almost unchanged intensity on the 545nm peak for higher temperature values, which can be seen on figure 1.2.7.

The Fluorescence Intensity Ratio (FIR) of these two peaks (525 nm and 545 nm) is given by the equation 1.10, where I_{525} and I_{545} are the intensity values of each peak, ΔE is the energy gap between coupled energy levels of $^2H_{11/2}$ and $^4S_{3/2}$, C is a constant related to other details on the transition, such as states degeneracy and emission cross-section, and k and T are the Boltzmann constant and temperature, respectively [Cao et al., 2015].

$$FIR = \frac{I_{525}}{I_{545}} = C\exp\left(\frac{-\Delta E}{kT}\right) \tag{1.10}$$

Having an exponential relation between FIR values and Temperature, the final step is

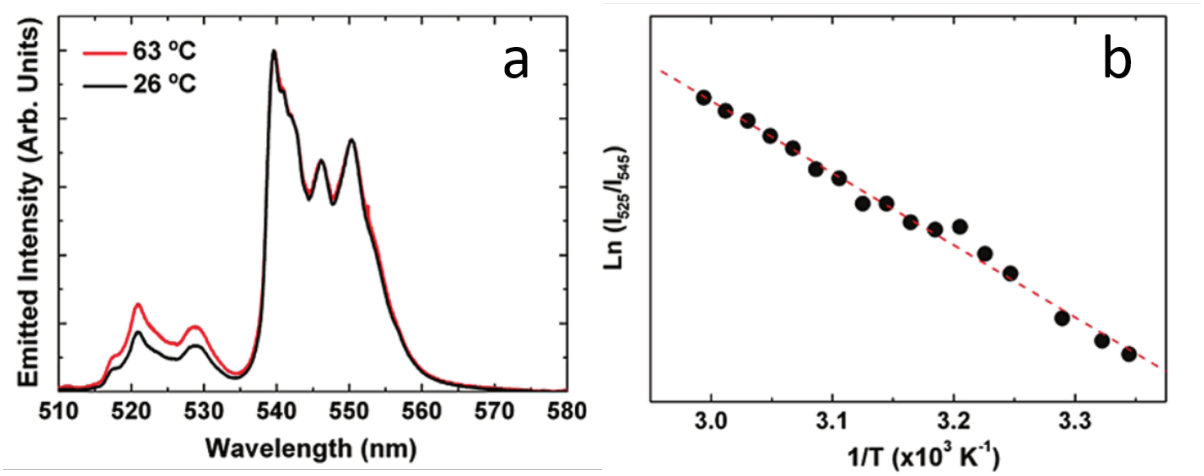

Figure 1.2.7 – **(a)** Comparison of $NaGdF_4:Er^{3+},Yb^{3+}$ spectra (510-580 nm region) at 26ºC and 63ºC. **(b)** Plot of Ln(FIR) against T^{-1}. The distribution is linear as predicted by equation 1.10. Extracted from [Vetrone et al., 2010]

to measure the fluorescence spectra. For this, one needs a luminescence microscope. A common set-up used for FIR measurements of temperature dependent upconversion of $NaGdF_4:Er^{3+},Yb^{3+}$ is depicted in figure 1.2.8, which uses a 980 nm wavelength continuous laser source focussed into the sample, for pumping purposes, and an objective to gather the resulting fluorescence from the sample to be read by a spectrometer. In figure 1.2.8 is also depicted a second light source, in this case a Ar^+ laser beam at 488 nm, also for pumping, which is focussed onto the sample through the same confocal objective used for gathering fluorescence. In order to be able to use the same objective for both purposes, as well as to separate the important part of the fluorescence spectra from reflected and scattered light from the laser beams, a dichroic mirror was used.

Figure 1.2.7 presents a captured spectra and a plot of FIR for different sample temperatures, obtained using a set-up similar to the one in figure 1.2.8. As expected, for higher temperatures, the intensity of the peak at 525 nm increases and the plot follows an exponential distribution.

To apply this technique for local temperature measurement during 3D DLW, a set-up made of a 3D DLW system with a fluorescence microscope is needed. Mueller *et. al* presents

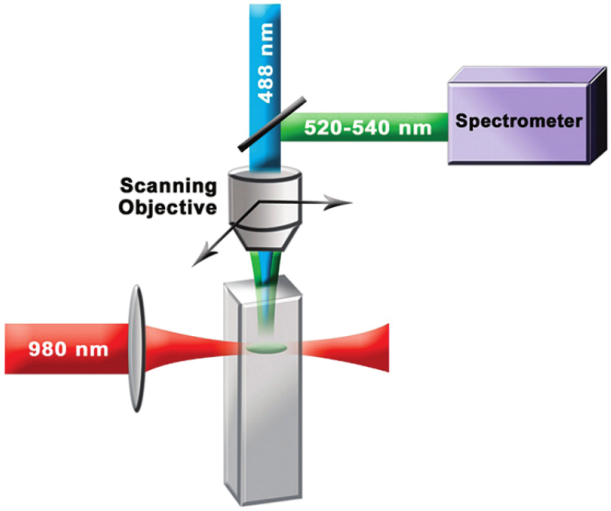

Figure 1.2.8 – Scheme of a common set-up used for FIR measurements using UCNCs doped samples. **(Red)** 980 nm continuous laser source, focussed through a lens into the sample, for pumping. **(Blue)** second pumping laser source, an Ar^+ 488 nm laser beam. **(Green)** the resulting UCNCs fluorescence, guided to a spectrometer. Extracted from [Vetrone et al., 2010].

an approach on this topic by developing the experiment seen in figure 1.2.9 [Mueller et al., 2013]. In this set-up we can see the use of a writing laser (810 nm fs-Ti:Sa laser), for material processing, and a second laser (980 nm diode laser) for UCNCs pumping. Both of these lasers are focussed onto the sample through the same confocal objective, for optical alignment sake, guaranteeing that the pumped UCNCs are the ones in the focal volume of the writing laser. The same confocal objective is used to gather fluorescence, which is then guided to a fibre-coupled spectrometer.

The sample lays on top of a piezo scanning stage, for precise XY movement, and is held by a temperature-controlled sample holder, for taking FIR measurements at different temperatures. A photo-diode camera was also used to visually follow the polymerization process, a common practice in 3D DLW.

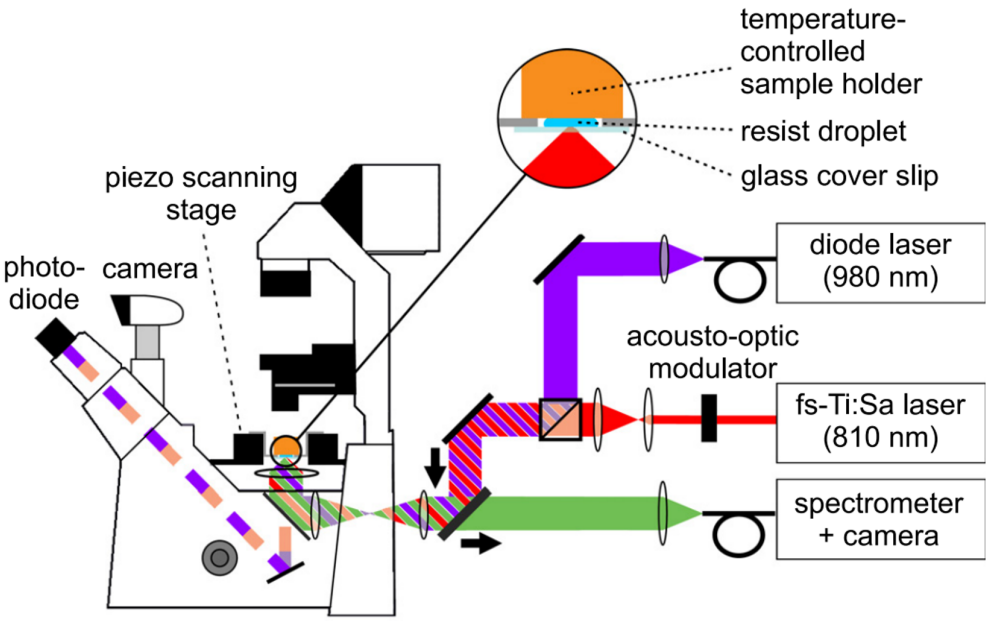

Figure 1.2.9 – Schematics of the set-up used in [Mueller et al., 2013] for *In-situ* local temperature measurement during 3D DLW. Extracted from [Mueller et al., 2013]

The resulting data of local *in-situ* temperature measurements, using this set-up, is presented in figure 1.2.10, alongside other experimental data using a similar approach [Varapnickas et al., 2018]. The measured *in-situ* local temperature during 3D DLW differs for both data shown (in more than 10ºC), which may be explained by the use of different photoresists (pentaerythritol triacrylate for fig. 1.2.10(a), and SZ2080 for 1.2.10(b)) but might also be related to the fact that the first (fig. 1.2.10a) had photoinitiator doped photoresist while the former (fig. 1.2.10b) used pure (undoped) photoresist.

In this work we will test this hypothesis of different local temperature values for pure and photoinitator doped photoresists during direct laser writing. The processes and techniques used in both works cited above [Sun and Kawata, 2004, Varapnickas et al., 2018] serve as a main base for the development of this dissertation.

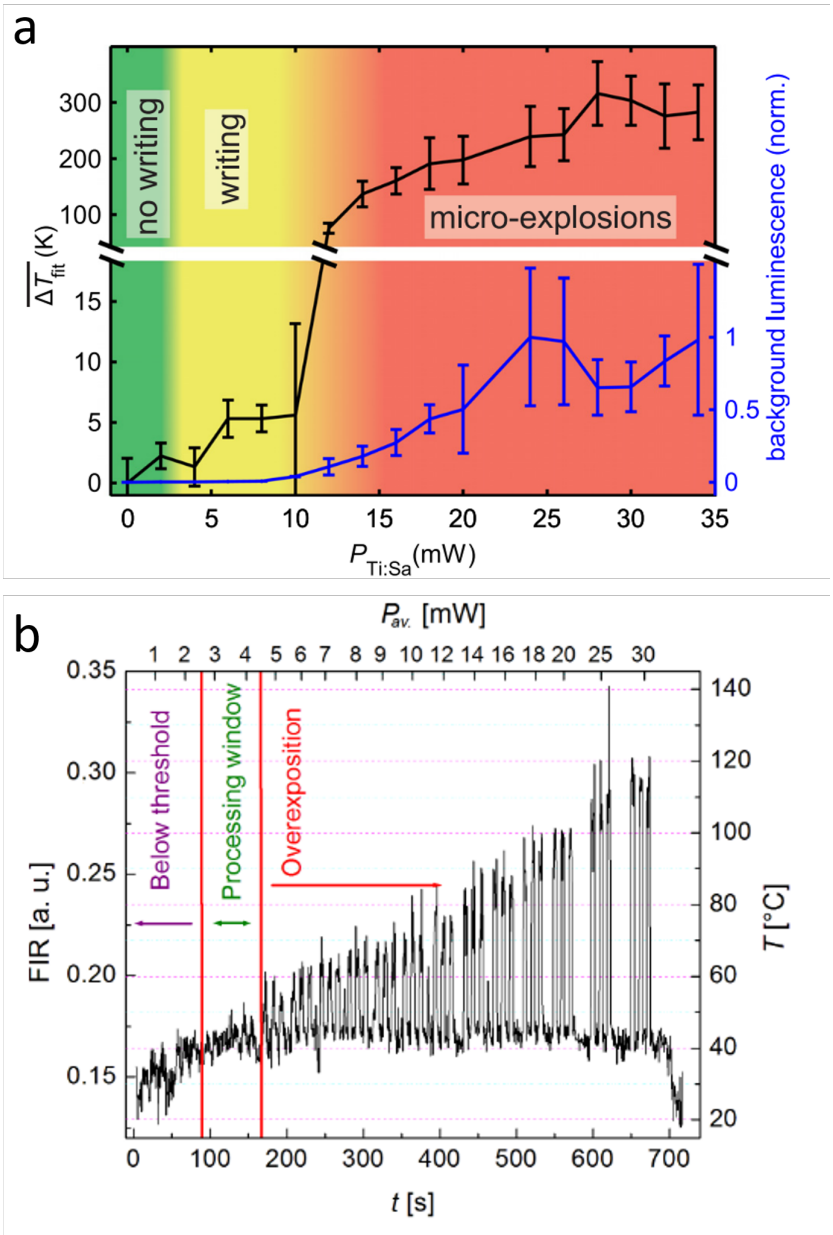

Figure 1.2.10 – Experimental data for *in-situ* local temperature measurements during 3D DLw. Different photoresists were used in both experiments (pentaerythritol triacrylate and SZ2080 respectively).**(a)** Plot of temperature variance from initial sample temperature for increasing writing power. Background luminescence comes from *Irgacure 819* photoinitiator. Extracted from [Mueller et al., 2013]. **(b)** Plot of absolute sample temperature (in °C) for increasing writing power. Exctracted from [Varapnickas et al., 2018].

Chapter 2

Experimental Methods

2.1 Designing the experimental set-up

In order to build a system that is able to accurately gather fluorescence spectra, while writing in-depth structures in polymer, one needs a design joining both a 3D DLW set-up (fig. 1.2.1) and a luminescence microscope (fig. 1.2.8). This is accomplished by the schematic layout used for the development of this work, presented in a simplified scheme in figure 2.1.1.

Adapted from the design used by [Mueller et al., 2013] described in fig. 1.2.9, this experimental set-up of fig. 2.1.1 can be separated into its two main parts, based on the function they serve: ***Laser Writing*** or ***Fluorescence Gathering***. In this chapter we will focus on each of these two parts in more detail, and how to properly combine them.

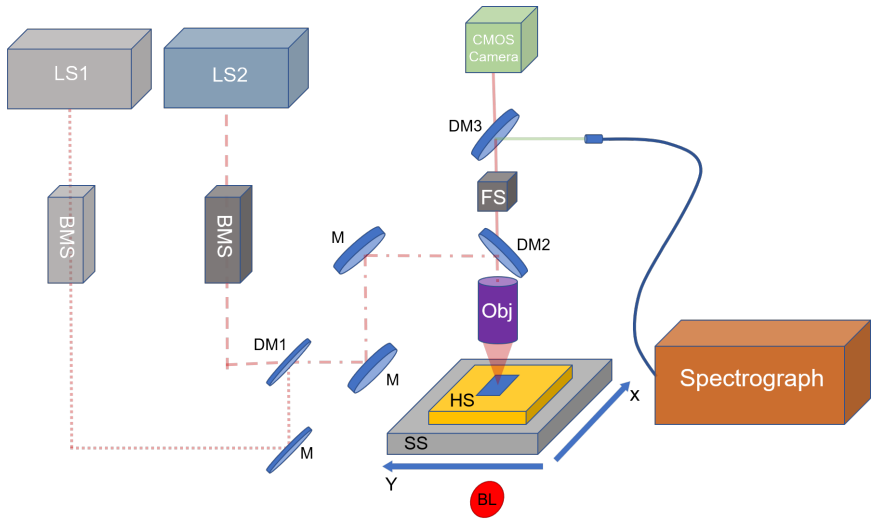

Figure 2.1.1 – Schematic image of the main experimental layout used in this work. Legend: **(LS1)** 1026nm Writing Laser Source **(LS2)** 975 nm Pumping Laser Source **(BMS)** Beam manipulation system **(M)** HR mirrors **(DM)** Dichroic mirrors **(Obj)** Objective **(FS)** Filtering **(HS & SS)** Heating and scanning stages **(BL)** Backlighting

2.1.1 Laser writing

The set-up part responsible for laser writing can be described as a system consisting of a laser source, delivering the laser beam, an eventually needed manipulation of the beam characteristics (such as divergence and power), and a microscope objective for beam focussing onto the sample. 3D Direct Laser Writing layouts also have a scanning stage to move the sample while being processed, and an imaging system to capture live images of the sample during the writing procedure. These components are assembled together as described in the scheme of fig. 2.1.2. In this section we will focus on the specifications for each elements based on the requirements for this particular application.

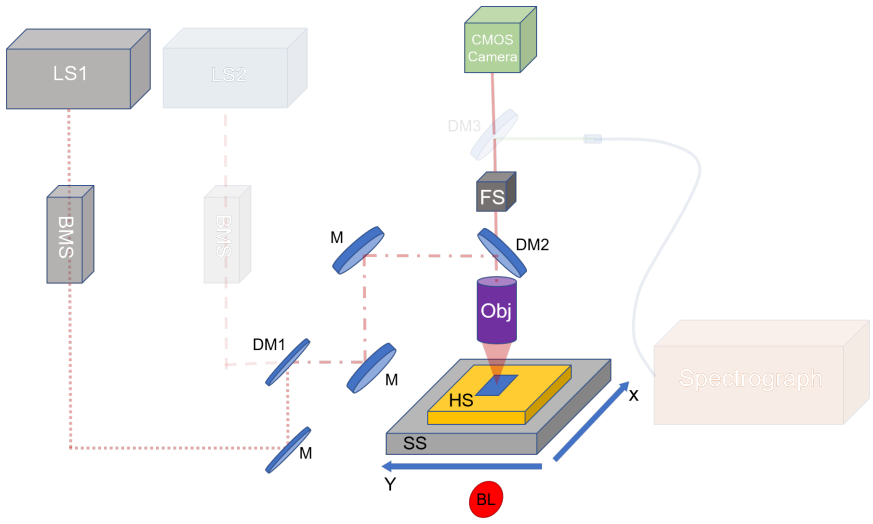

Figure 2.1.2 – Schematic image of the laser writing set-up layout used in this work Legend: **(LS1)** 1026 nm Writing Laser Source **(BMS)** Beam manipulation system **(M)** HR mirrors **(DM)** Dichroic mirrors **(Obj)** Objective **(FS)** Filtering **(HS & SS)** Heating and scanning stages **(BL)** Backlighting

Laser source for writing: For the writing laser source a *PHAROS* femtosecond laser was used. The laser was set to a frequency of 200 *kHz*, a pulse duration of 300 fs and an output wavelength of 1026 nm. This particular laser source was already in use as the main laser source for nano-lithography applications in the lab, therefore the set laser conditions were chosen based on the polymerizing results obtained in previous samples. A characteristic of the laser beam that could not be measured with the necessary precision, although it is relevant for this implementation, was the beam divergence. Beam divergence changes the beam width along the optical path and influences the focussing depth in the sample. A simple, though inefficient, method of measuring the beam width at different distances from the laser was used, giving an approximate value of $5\text{x}10^{-3}$ rad. Other more precise methods could be used for this particular measurement, such as the knife-edge method [de Araújo et al., 2009].

Laser beam manipulation: Positioned after the laser source, and before the objective lens, a software-controlled system composed by a mechanical laser attenuator and a power-meter was used. This enables the selection of an exact laser power delivered to the sample at

any time. One can see in fig. 2.1.3 a set of lines written at different power values.

After being reflected through several mirrors, including two dichroic mirrors (DM1 and DM2 - fig. 2.1.2), the laser is focussed through the microscope objective. The dichroic mirrors used were a 100 nm cut-off wavelength short-pass DM (DM1 - fig. 2.1.2), to unite the the two laser beams (writing and pumping), and a 850 nm cut-off wavelength short-pass DM (DM2 - fig. 2.1.2), to separate the laser path from the gathered light path. The laser reaches the microscope objective with a visible beam diameter of ~ 4.2 mm, overfilling the objectives diameter of 3.4 mm. By using the full diameter of the microscope objective, we increase the numerical aperture of the system to its maximum value (the specified numerical aperture value of the objective).

Microscope objective: The microscope objective used was a 50X *Mitutoyo* Plan Apochromatic NIR Infinity Corrected Objective with a numerical aperture(NA) = 0.42. Usually, for 3D Direct Laser Writing processes, microscope objectives with higher NA values or even specially designed lens systems for 3D Direct Laser Writing are used [Burmeister et al., 2012b, Fuchs et al., 2006, Burmeister et al., 2012a]. For this work, the choice of objective was limited by the fluorescence gathering requirements, as we will see in the next section (section 2.1.2).

Aspects of the focussed laser beam: Even though polymerization using this objective is possible (fig. 2.1.3), due to its low NA value (0.42) the laser beam focal volume inside the photoresist will be larger and more elongated when compared to 3D DLW using high-NA objectives [Zhan, 2016]. The dimensions of the focal volume inside the photoresist sample can be estimated using the following equations, based on the Rayleigh criterion for diffraction limit:

$$dxdy = 1.22\frac{\lambda}{\mathrm{NA}} \qquad (2.1) \qquad\qquad dz = 2\frac{\lambda.n}{\mathrm{NA}^2} \qquad (2.2)$$

where NA is the objectives numerical aperture, λ is the laser wavelength and n is the refractive index of the photoresist. [dx,dy] are the transverse dimensions and [dz] is the axial dimension (the direction of the laser). For the conditions of this work, the calculations for

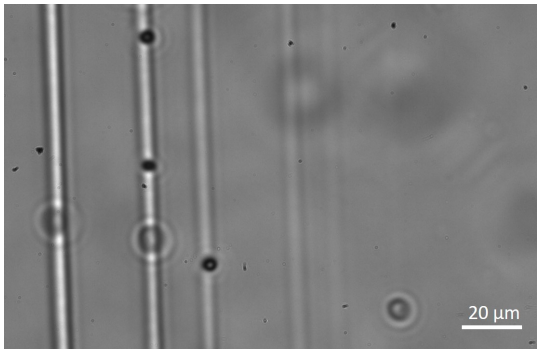

Figure 2.1.3 – Set of lines written on SZ2080 photoresist with the *PHAROS* laser focussed through the *Mitutoyo* microscope objective at different writing power values (left→right, decreasing power). Image captured with the CMOS camera.

the dimensions of the focal volume are dx = dy = 2.77 μm and dz = 18.18 μm, giving us the shape presented in fig. 2.1.4. It is important to notice that, even though the voxel is created inside this volume and may share an approximate shape and size (depending on laser power and exposure time), it does not represent the voxel itself.

Scanning stage and imaging camera: The used scanning stage was a 8MTF - Motorized XY Scanning Stage from *Standa*, with a full step resolution of 2.5 μm and a 1/8 step of 0.81 μm. Step-motors are not a regular choice for 3D DLW assemblies, and are usually replaced by piezo-stages that can achieve nanometer step resolutions, but for this application, where the focal volume smallest dimension is around 3 μm, high scanning precision is not required. For imaging, a simple DMK 22AUC03 CMOS camera from *The Imaging Source*® camera was used together with a simple lens (~200 mm focal length) for focussing onto the camera sensor plus a LED for backlightning.

2.1.2 Fluorescence gathering

The experimental set-up part responsible for fluorescence spectra gathering is composed by a laser source, for upconversion pumping, the same objective lens used in the previous section (laser writing), a filtering system and finally a spectrometer or spectrograph to analyse the fluorescence spectra. In order to run temperature calibrations a heating stage will

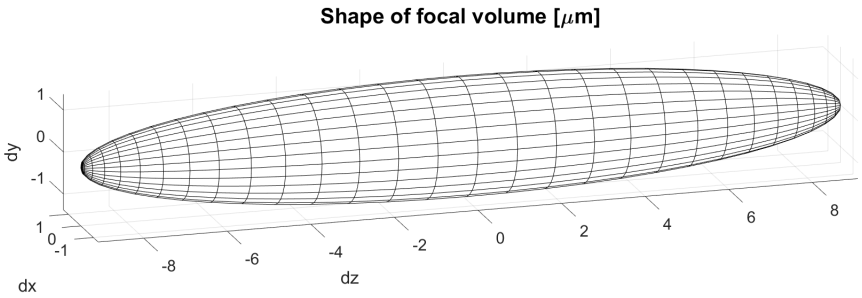

Figure 2.1.4 – Focal volume dimensions calculated by equations 2.1 and 2.2 using λ=1026 nm (writing laser wavelength), NA=0.45 (objectives numerical aperture) and n=1.8 (refractive index of SZ2080 photoresist, main component of our samples).

also be added to this set-up. All of the components are mounted as depicted in the scheme of fig. 2.1.5. In this section we will focus on the specifications for each of these elements based on the requirements for this particular application.

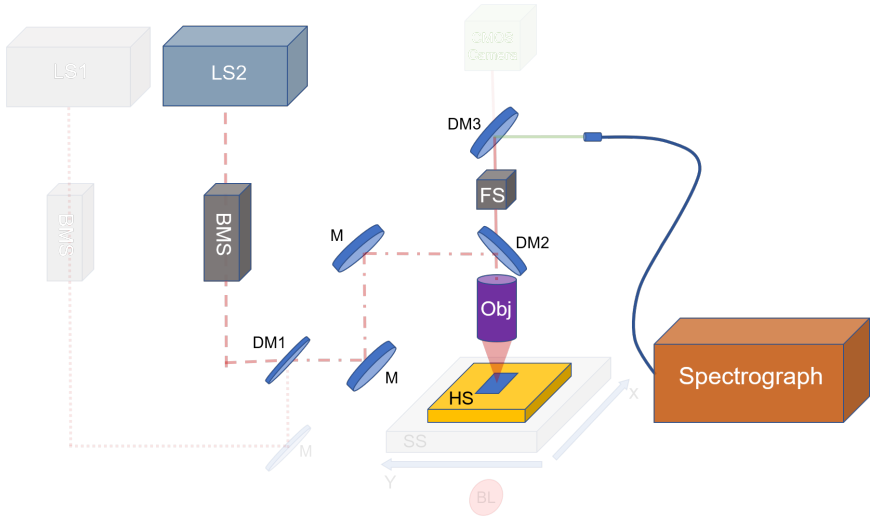

Figure 2.1.5 – Schematic image of the fluorescence gathering set-up layout used in this work. Legend: **(LS2)** 975 nm Pumping Laser Source **(BMS)** Beam manipulation system **(M)** HR mirrors **(DM)** Dichroic mirrors **(Obj)** Objective **(FS)** Filtering **(HS & SS)** Heating and scanning stages

Laser source for pumping: The upconversion process, in which we rely to gather the temperature dependent fluorescent spectra, starts by pumping the UCNCs with a laser source. In our set-up a 80 *MHz*, 300 *fs* pulse laser Oscillator was used, set to the wavelength needed for the pumping process described in section 1.2.1 - 975 nm center wavelength. As one might guess, this laser is not the perfect solution for pumping photoresists doped with UCNCs due to its short pulse duration, which might result in an instant photon intensity capable of polymerizing the sample, depending on the delivered power - as seen in fig. 2.1.6. Besides that, UCNCs containing Yb and Er will experience self-heating when the pumping power exceeds 40mW (pumped-induced heating) [Xu et al., 1998]. For this step of the process, a CW (continous wave) laser is usually used instead of a pulsed laser in order to reduce the instant power delivered to the UCNCs, and so, all the undesired effects that follows. For lack of one, the laser Oscillator was used reducing its output power ($\sim$ 600 mW) to a minimum value of 1 mW (measured with a powermeter after the microscope objective) recurring to a neutral density filter. At this power (1 mW) the polymerization seen on fig. 2.1.6 was no longer present but, since the peak power is still high above the 40 mW threshold (peak power ~417 W). Even if the laser Oscillator pulse lasts an extremely short period of time (300 *fs*), one cannot predict the result it might have on pumped-induced heating. Further decrease in power its not advised for it will result in low fluorescence intensity.

Laser beam manipulation: Besides the already mentioned neutral density filter for laser power attenuation, a telescope was also built and used for two main reasons: to reduce beam divergence and to guarantee a spot size of approximately 3.4 mm when reaching the microscope objective in order to use its full working area (of the microscope objective). This was only possible because the initial values for beam divergence, spot size at a known distance and M^2, along with other values, were studied with a beam profiler. The designed telescope uses two bk7 optical glass lens, separated by 12.5 mm, with focal distances of +200 mm and -200 mm and it was positioned at 89 *cm* from the laser Oscillator exiting channel. This reduces the greatest initial beam divergence of 0.7 *mrad* to 0.25 *mrad* and guarantees a beam

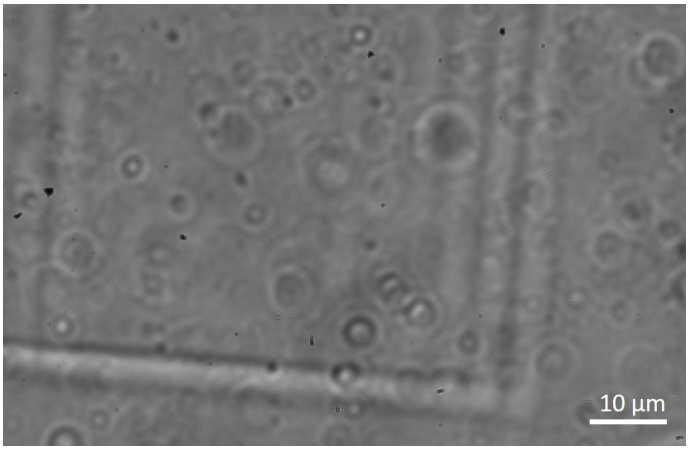

Figure 2.1.6 – Polymerized material after 90min of exposure to the laser Oscillator at 40mW, while scanning a repetitive square pattern. Sample: SZ2080 + $NaGdF_4$:Yb^{3+},Er^{3+} UCNCs [w/w] 15:1 (more info on section 2.2).

diameter of 4.0 mm when reaching the microscope objective. This telescope was designed and optimized using *OSLO* software.

Microscope objective: Even though the used objective and some of its characteristics were already mentioned in section 2.1.1, the 50X *Mitutoyo* Plan Apochromatic NIR Infinity Corrected Objective was mainly chosen due to the advantages it brings for gathering the fluorescence light coming from the sample. It has a 520 - 1063 nm wavelength range with a transmission rate of about 70%, which includes the 525 nm and 545 nm fluorescence wavelengths we want to study. Additionally, this objective is a plan apochromatic, corrected from 480 to 1800 nm, guaranteeing that both lasers (for writing and pumping) will be focussed at the same distance, despite their different wavelengths. This also means that the fluorescence will be gathered from the same position as the focal volumes of both lasers, as intended.

Due to the proximity of wavelengths of both lasers used (1026 nm and 975 nm), it is safe to assume that the focal volume depicted in fig. 2.1.4 also applies to the shape of the pumping laser focal volume (with a difference of less than 0.15 μm in both axial - dz - and transverse - dxdy - dimensions). Together with the fact of being focussed at the same distance, the volume of material being pumped at the focal volume of the pumping laser coincides (if the beams are aligned) with the focal volume of the writing laser. The green fluorescence light

emitted by laser-pumped $NaGdF_4$:Yb^{3+},Er^{3+} UCNCs can be seen in the photo of fig. 2.1.7

Filtering: The gathered light from the microscope objective is filtered by three sequential colour glass filters: BGG24, BGG23, BGG21 by *Altechna Co. Ltd.*, working as a short-pass filter, filtering any undesired wavelengths that may still exist while maintaining about 70% of the fluorescence leaving the objective as well as some red light from the backlighting LED. A second filtering step is made in the long-pass dichroic mirror (605 nm cut-off wavelength, DM3 - fig. 2.1.2) which separates the fluorescence from the red LED light for imaging.

For spatial filtering, the fluorescence light is focussed (using a convex bk7 optic glass lens with +100 mm of focal distance) into an optic-fibre with a 200 μm diameter core, working as a large pin-hole. This does not work as a very effective spatial filter, having a diameter 100 times larger than the transverse dimensions of the focal volume.

Spectrograph: The spectrograph used for this implementation was a *SpectraPro HRS 300* by *Teledyne Princeton Instruments* with a mounted ultra-low noise CCD array camera [1]. Due to the low intensity fluorescence gathered from the sample, a highly sensitive spectrograph is important in order to capture the most light possible. This enables lower pumping powers while maintaining a high temporal resolution (to capture small events such as micro-explosions due to burning of the sample). Three lines of the CCD camera array were used in order to optimize the amount of light captured. An example of a captured sample spectra using this spectrograph set with an integration time of 150 ms is depicted in fig. 2.1.8.

In spite of the efficiency of this spectrograph in the capture of light, all the measurements have to be made in complete darkness, including turning off the LED backlight.

Heating Stage For temperature calibrations, a *Linkam* PE120 heating stage was mounted above the scanning stage. This heating stage enables a 0^{o}C to 120^{o}C temperature calibration with a precision of $\pm$0.1^{o}C.

[1] Since the used spectrograph is not fibre-coupled, the end of the optic-fibre had to be mounted pointing to the window of the spectrograph

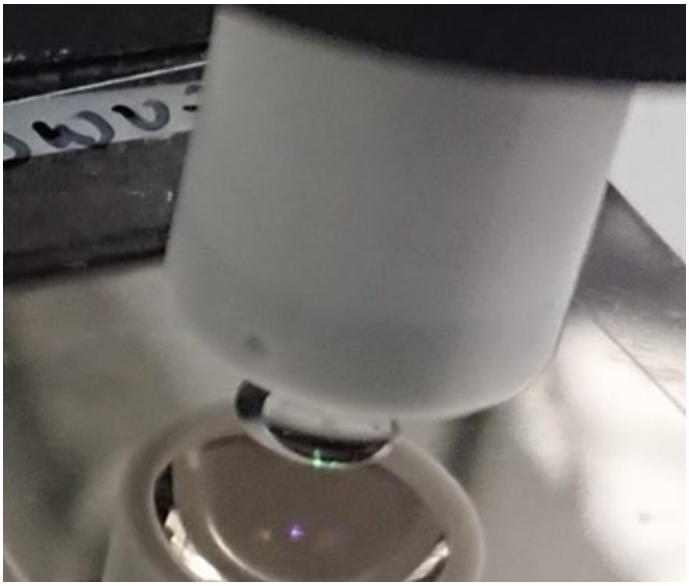

Figure 2.1.7 – Green fluorescence light emitted by laser-pumped $NaGdF_4$:Yb^{3+},Er^{3+} UCNCs.

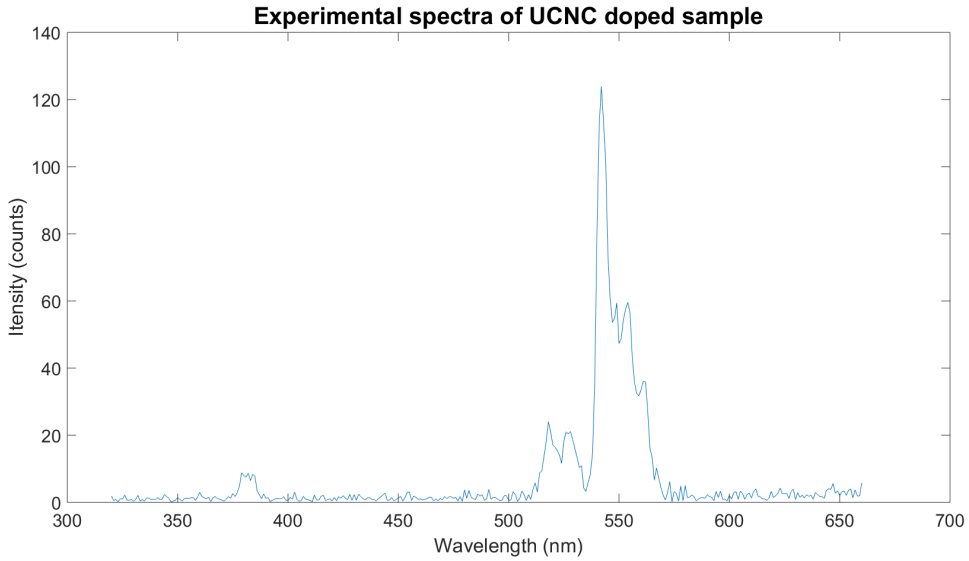

Figure 2.1.8 – Spectra from sample captured by spectrograph. Integration time: 150 ms. Sample: SZ2080 + $NaGdF_4$:Yb^{3+},Er^{3+} UCNCs [w/w] 80:1 (more info on section 2.2). Even with a low amount of counts (~ 20 for the peak at 525 nm and ~ 120 for the peak at 545 nm) the expected spectra form the UCNCs is easily distinguishable.

2.1.3 Optical alignment of the system

One of the most important aspects of this set-up is its alignment. In order for the experiment to be successful, a number of steps have to be done to guarantee a properly aligned system. This work relies on having two confocal laser beams (the writing and pumping laser), focussing on the same spot in the sample through the same microscope objective, and so a μm precision alignment is required. Also, due to the low fluorescent emitted by the sample, it is very important to do a thorough alignment of every component leading the fluorescence light from the objective to the spectrograph, in order to reduce losses.

To align each laser beam with the objective, a system of mirrors is used in combination with at least two IR fluorescing alignment targets. After each laser beam is set to its desired path, reaching the microscope objective, one must guarantee that both beams are focussing on the same spot in the sample. This is easily made by taking advantage of the problem regarding undesired polymerization by the laser Oscillator presented in fig. 2.1.6. After polymerizing one voxel with each laser (by increasing the laser Oscillator power), the misalignment of the two beams becomes visible - fig. 2.1.9**(a)** - and can then be corrected (always maintaining the laser beams aligned with the centre of the microscope objective). Once the two beams are aligned, only one voxel (seen on camera images as a white spot) appears in the material -fig. 2.1.9**(b)**.

2.2 Sample preparation

The samples used in this work will be composed by up to three materials: the photoresist as the main base, pure or doped with photoinitiators, to which a dose of upconverting nanocrystals is added. In this section we will be focussing on how to correctly prepare the UCNCs doped photoresists, resulting in samples that generate enough fluorescence for FIR measurements without jeopardizing the polymerization mechanism.

The chosen photoresist was SZ2080, an organic-inorganic hybrid compound included in

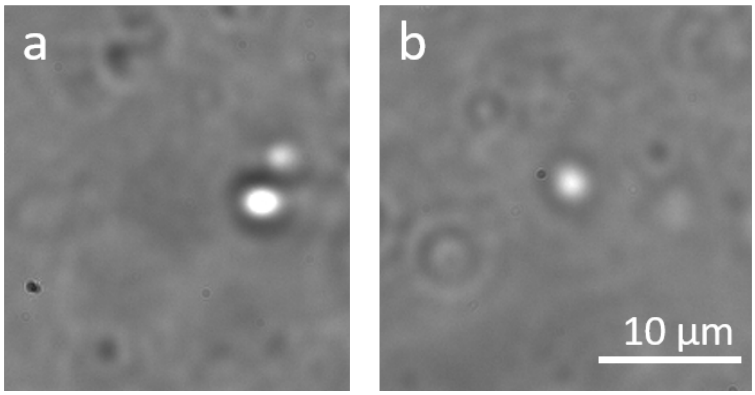

Figure 2.1.9 – Alignment procedure by polymerizing the sample with each beam. **(a)** Misaligned system - two different polymerized spots can be seen. **(b)** Aligned system - only one polymerized spot can be seen, which means both beams are focussing on that same spot.

the organically modified silicate (ORMOSIL) material class [Ovsianikov et al., 2008] - molecular structure seen in fig. 1.2.4. SZ2080 is widely used for 3D DLW, gaining its popularity due to the ultra-low shrinking and rigid mechanical properties after polymerized [Malinauskas et al., 2013, Malinauskas et al., 2010, Malinauskas et al., 2016, Žukauskas et al., 2016], in addition to being biocompatible, enabling *in-vivo* applications [Danilevičius et al., 2013]. SZ2080 is a negative-tone photoresist, meaning that it becomes less soluble for a certain developing solvent. In the case of organic-inorganic hybrid materials, such as SZ2080, the solvent used is generally isopropanol. Photoresist SZ2080 was acquired from FORTH, IESL (Heraklion, Greece) and the synthesis procedure of the photoresist can be found in [Ovsianikov et al., 2008].

SZ2080 absorbs radiation in the wavelength proximity of 390 nm, meaning that the nm wavelength writing laser we are using does not polymerize using multi-photon absorption processes, laying in between the two-photon and three-photon polymerization wavelengths - 780 nm and 1170 nm, respectively. For pure SZ2080 it is safe to assume that only polymerization through avalanche ionization is present. To improve the laser-photoresist interaction and increase the rate of multi-photon polymerization, some of the SZ2080 samples were doped with *Irgacure 369* photoinitiator (PI).

Irgacure 369, one of the most common photoinitiators on the market, has its highest

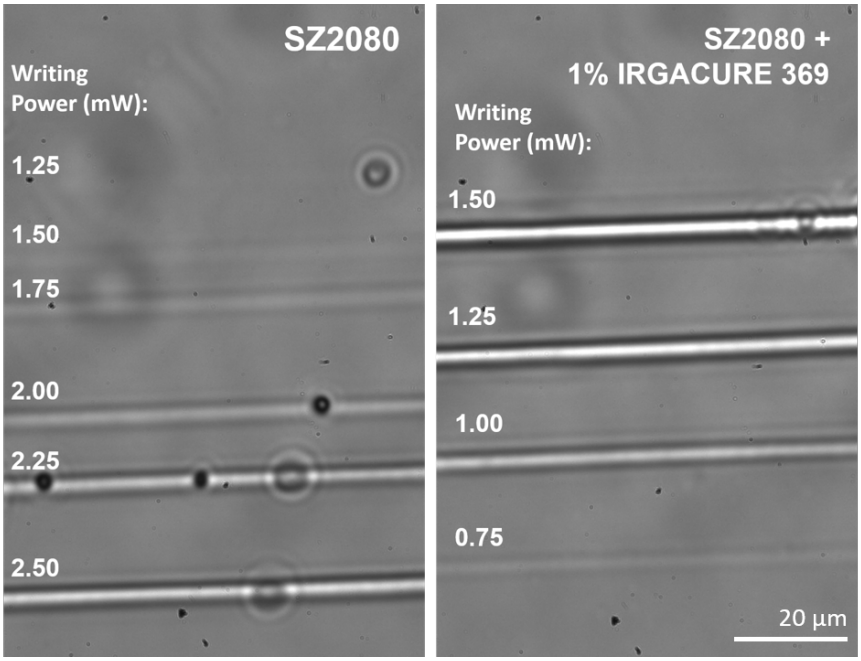

Figure 2.2.1 – Comparison between lines written at the same writing power in pure and PI doped SZ2080. All lines were written at the same writing speed of 10 μm.

value of absorption for 350 nm wavelengths, and it presents a TPA cross-section of 7 *GM* (1 $GM = 10^{-50}$ cm^4 s photon^{-1}) for wavelengths of 650 nm, being a common choice of photoinitiator for 3D DLW polymerization applications using shorter writing wavelengths [Schafer et al., 2004]. For the case of the 1023 nm writing laser wavelength, the 3PA (three-photon absorption) process will be the main non-linear absorption mechanism. Even though there is no experimental data for the 3PA cross-section of *Irgacure 369*, one can visualize the influence of this photoinitiator while writing on doped photoresist, comparing it to the same writing effects on pure material. In fig. 2.2.1 we can see that the writing power needed to produce the same structures as in pure SZ2080 is reduced to half for a sample of SZ2080 doped with 1% of *Irgacure 369* ([w/w], weight to weight ratio).

To sense the local *in-situ* temperature of the sample while being processed, there is a need of doping the SZ2080 with upconverting nanocrystals (UCNCs). In this work $NaGdF_4$: Yb^{3+}, Er^{3+} UCNCs were used due to their high upconversion efficiency. As presented in 1.2.1, $NaGdF_4$: Yb^{3+}, Er^{3+} nanocrystals have one of the highest upconversion efficiency, translating

to higher fluorescence intensities. The synthesizing procedure of these $NaGdF_4$: Yb^{3+}, Er^{3+} nanocrystals can be seen in [Baziulyte-Paulaviciene et al., 2017, Varapnickas et al., 2018]. For this work, the nanocrystals used were synthesised by the Faculty of Chemistry and Geosciences of Vilnius University. Further characterization of this material can be seen in [Varapnickas et al., 2018].

The exact synthesized material used was $NaGdF_4$: Yb^{3+}, Er^{3+} core nanocrystals, surrounded by a shell of pure $NaGdF_4$ - $NaGdF_4$: Yb^{3+}, Er^{3+} @$NaGdF_4$ - with a mean average size of 12 nm. The core-shell architecture enhance emitted fluorescence from the nanocrystals core, by diminishing exterior molecular influence in the upconverting process [Baziulyte-Paulaviciene et al., 2017]. These nanocrystals are conserved in a toluene suspension with a concentration of 40g of UCNCs per ml in order to prevent agglomeration, thus preserving the 12 nm size particles.

The process of preparing UCNC doped samples has to take into consideration the influence that UCNC concentration has during laser writing. High UCNC concentration in the sample results in a higher number of pumped UCNCs per volume, enhancing overall fluorescence intensities, but it also affects SZ2080 polymerization mechanisms, as seen fig. 2.2.2. In this work we will be using SZ2080+UCNCs with a 80:1 [w/w] ratio, which was an optimal value both for fluorescence intensity and influence in the writing process.

To prepare a sample of SZ2080+UCNC 80:1 [w/w], one starts to add 25 μl of the 40 mg/ml suspension of $NaGdF_4$: Yb^{3+}, Er^{3+} @$NaGdF_4$ in toluene, to 186 mg of a solution of SZ2080 dissolved in isopropanol (43:67 [w/w]). The resulting liquid solution is stirred in a magnetic stirrer for 6 hours minimum, to break eventual aggregated groups of UCNCs and homogenize the UCNCs distribution in the solution. After the magnetic stirrer, a small drop of solution (~6 mul) is dropcasted on a microscope slide and it is pre-baked at 90ºC for the isopropanol and toluene to evaporate, leaving us with a gel-type drop of SZ2080+UCNCs 80:1 [w/w] ratio. The pre-baking process cannot expose the dropcasted solution to an immediate temperature of 90ºC, risking to dry the surface of the drop thus disabling the evaporation of

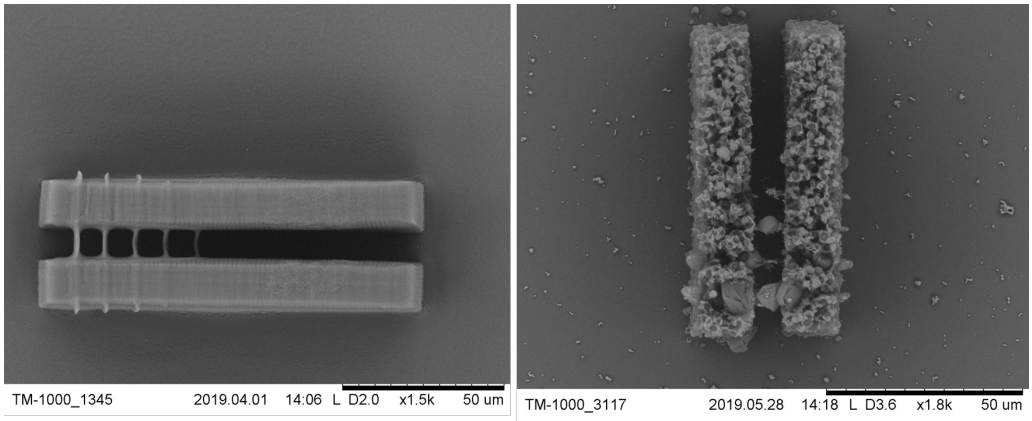

Figure 2.2.2 – Scanning Electron Microscope images of two structures built with a NA=0.8 microscope objective. **(Left image)** Structure built on pure SZ2080 photoresist. **(Right image)** The same structure built on SZ2080+UCNC 25:1 [w/w]

the solvents inside the drop, so it is made in a process of increasing the baking temperature in slow steps (e.g. 40ºC for 10 min / 60ºC for 20 min / 75ºC for 45 min / 90ºC for 90 min / 75ºC for 10 min / 40ºC for 10 min). Two main samples were prepared using this method, one SZ2080+UCNCs 80:1 [w/w] and the second with an already *Irgacure 369* photoinitiator doped solution of SZ2080: (SZ2080+1%IRG)+UCNCs 80:1 [w/w]. The main samples used in this work as well as their composition are presented in table 2.1.

Table 2.1 – Table of approximate weight composition of the samples used in section 3.

Samples:	Approx. fraction of total sample weight (%)		
	SZ2080	Irgacure 369 PI	$NaGdF_4$:Yb^{3+},Er^{3+} @$NaGdF_4$
Pure SZ2080	100.0	-	-
SZ2080+1%IRG	99.0	1.0	-
SZ2080+UCNCs	98.8	-	1.2
(SZ2080+1%IRG)+UCNCs	97.8	1.0	1.2

Although the SZ2080+UCNCs 80:1 [w/w] and (SZ2080+1%IRG)+UCNCs 80:1 [w/w] samples were considered to present a similar behaviour to laser writing as their UCNCs undoped counterparts (Pure Sz2080 and (SZ2080+1%IRG)+UCNCs), the influence of the UCNCs in the material is still present. Figure 2.2.3 depicts structures fabricated using SZ2080+UCNCs 80:1 [w/w] where it is easily visible that the overall structural integrity of the fabricated structure is compromised. Also in figure 2.2.4, during the laser writing of lines on SZ2080+UCNCs 80:1

[w/w] some micro-explosions (black spots) occurred while writing that segment of the line.

Isolated micro-explosions in the sample might result from a high concentration of UCNCs in a specific volume of the material. Although $NaGdF_4$: Yb^{3+}, Er^{3+} nanocrystals have a low absorption rate for the specific wavelength of 1026 nm, due to the high peak power of the pulses, an agglomerate of UCNCs might still absorb enough for high heat to accumulate in a very small volume, thus burning the material. This effect happens more often in samples with higher concentration of UCNCs, explaining the defective structures of figures 2.2.2 and 2.2.3.

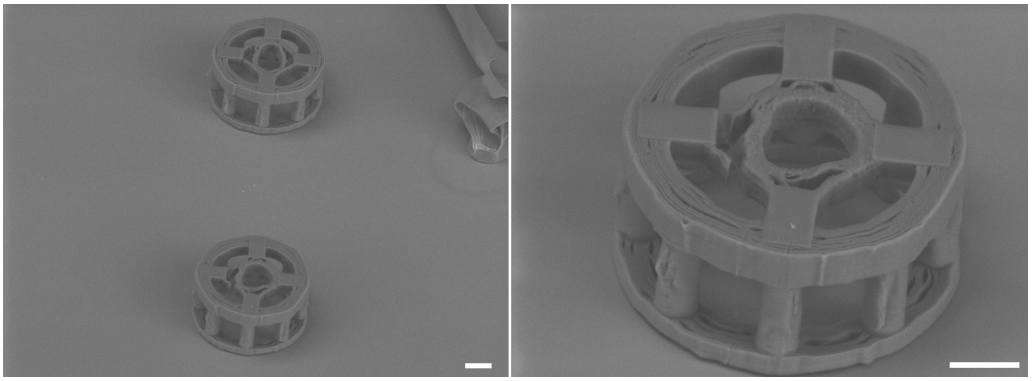

Figure 2.2.3 – SEM images of structures built with a NA = 0.8 microscope objective on SZ2080+UCNCs 80:1 [w/w]. Structural defects can be seen. Both scale bars are 10 μm.

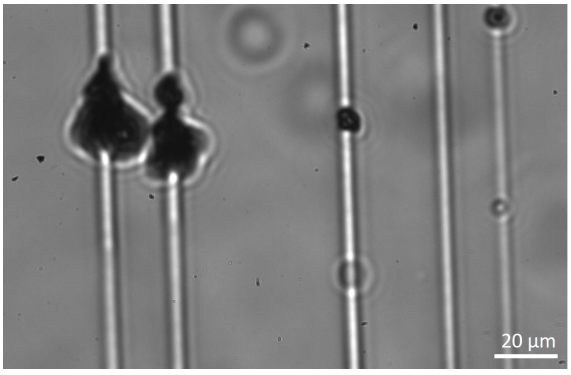

Figure 2.2.4 – Image of burnt spots (black areas) in lines written on SZ2080+UCNCs 80:1 [w/w]. Taken with the CMOS camera.

2.3 Spectra analysis and FIR measurements

After capturing the fluorescence from laser-pumped UCNC-doped samples (using the spectrograph) the next step is to analyse that spectra in order to calculate the FIR of the two peaks centred at 525 nm and 545 nm. As previously discussed in section 1.2.1, these two peaks are related to the upconversion process of the $NaGdF_4$:Er^{3+},Yb^{3+} nanocrystals, and their intensity ratio is what will enable local temperature measurements - see equation 1.10. A general spectra resulting from low-power laser-pumping both SZ2080+UCNC and (SZ2080+1%IRG)+UCNC is depicted in figure 2.3.1, where both fluorescent peaks are easily recognisable. Both peaks are far from sharply limited to their centre wavelength, 525 nm and 545 nm, and are spread over a range of wavelengths. This results in FIR calculations that are not a ratio between the peaks maximum intensities but between the areas under the peaks, by integrating on their wavelength range.

Literature presents two main ways of selecting the integration intervals used for FIR, one that integrates the peaks in their whole wavelength range, resulting in a experimental value for ΔE (the energy gap between the Er^{3+} coupled levels of $^2H_{11/2}$ and $^4S_{3/2}$ - section 1.2.1) similar to its tabled value [Varapnickas et al., 2018, Mueller et al., 2013], and another that only uses the wavelength range for which the intensity of the peak is greater [Aigouy et al., 2005]. The first case would integrate the peaks using the wavelength intervals [514 nm, 531 nm] and [538 nm, 565 nm], whereas for the second the intervals [514 nm, 531 nm] [538 nm, 551 nm] would apply. A visual representation of these two possible ways of integrating the peaks intensity for FIR calculations is depicted in figure 2.3.2.

Even though the first choice of integration intervals seems the most reliable in terms of scientific value, since it bases itself on the theory behind the upconversion process used in this work, the main drawback of integrating the whole peak comes from the fact that the shape of the spectra between 551 nm and 565 nm varies for different experimental conditions, such as UCNC concentration on the sample and pumping power - APPENDIX A. Since the exact UCNCs distribution is proven not to be homogeneous and the pumping power

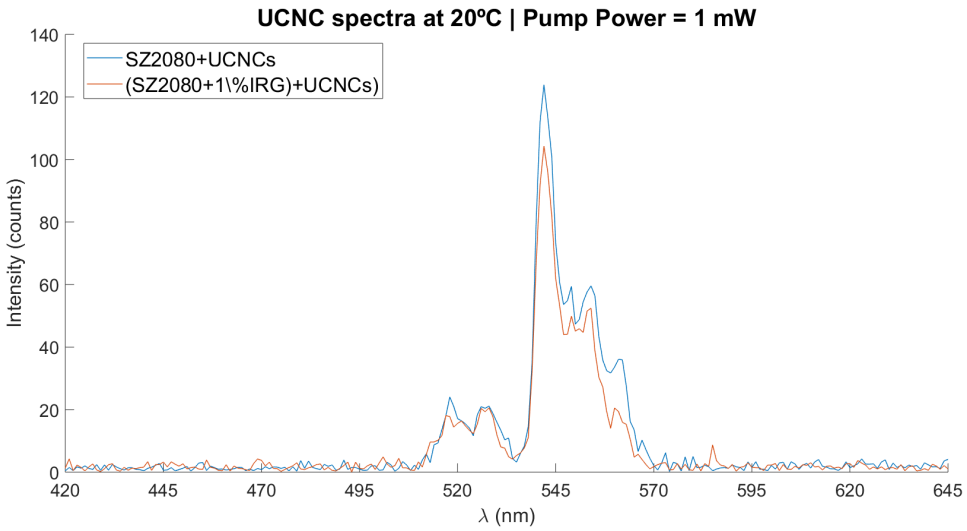

Figure 2.3.1 – Fluorescence spectra of both samples used in this work: SZ2080+UCNCs and (SZ2080+1%IRG)+UCNCs, while being pumped with a laser power of 1 mW.

might have small variances throughout the experiment, the FIR measurements on this work are taken using the shorter intervals: [514 nm, 531 nm] for peak centred at 525 nm and [538 nm, 551 nm] for peak centred at 545 nm.

2.3.1 Temperature calibration of FIR values

FIR experimental values are dependent on a variety of factors. These are not only related to the effect of the material surrounding the UCNCs on the upconversion process, but also to the optics used on the experimental set-up (e.g. varying transmission coefficients for different wavelengths). In order to bypass this, a temperature calibration of the FIR values is always needed, even for different samples using the same set-up.

For the temperature calibration, the sample was heated from 20ºC to 120ºC, in steps of 10ºC while being pumped by the laser Oscillator at a constant power of 1 mW. The sample was kept at a constant temperature for 3 min. in every step, during which the fluorescence spectra was collected. The integration time of the spectrograph was 150 ms, since that was the integration time intended to be used on the measurements while writing, resulting in 600 spectra gathered for every temperature step.

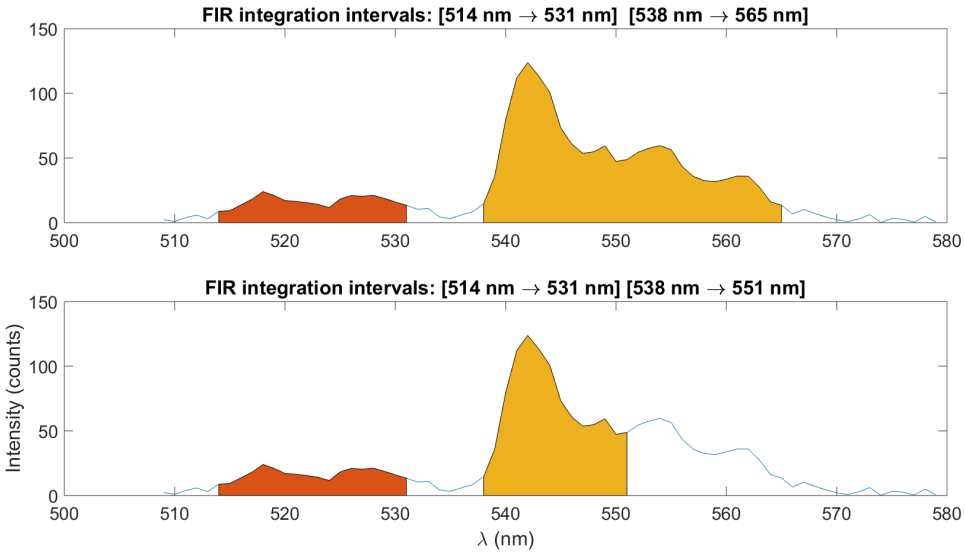

Figure 2.3.2 – Two possibilities of integrating peak intensity for FIR calculations using different integration intervals. **(Top)** Integration limits used in [Varapnickas et al., 2018, Mueller et al., 2013]. **(Bottom)** Integration limits used in [Aigouy et al., 2005] and the ones that will be used for FIR analysis in this work.

In order to reduce any local effects that might influence on the gathered spectra at a certain temperature, the temperature calibration was made while repetitively scanning the sample in a 25 μm x 25 μm square pattern, as seen in figure 2.3.3, at a velocity of 5 μ/s.

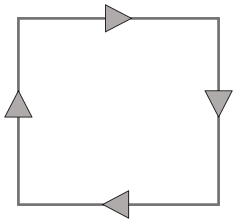

Figure 2.3.3 – Scanning pattern used during temperature calibration. A 25 μm x 25 μm square pattern scanned at a velocity of 5 μ/s.

2.3.2 FIR temperature measurements during direct laser writing

For spectra gathering while writing on UCNC doped samples, lines of 1 mm in length were scanned at a speed of 10 μm/s varying the writing power for each line. The lines were separated by at least 20 μm from each other to ensure a polymerization process surrounded

by pre-polymer for every line, maintaining identical conditions on every scan. The line pattern was selected in opposition to square patterns (like the one used for the temperature calibration) to guarantee an equal amount of exposition to the writing laser on every part of the sample, which cannot be obtained in patterns that contain corners. The lines were written as close as possible to the microscope slide (the optical path was objective → microscope slide → sample) to avoid fluorescence loss due to scattering and absorption by the surrounding material. All the laser powers used in this process were previously tested on the material in order to select a set of powers that would not damage the material by burning it, using the CMOS camera imaging for this purpose. As expected, laser powers used for polymerizing the (SZ2080+1%IRG)+UCNCs sample were lower than the ones used for the SZ2080+UCNCs.

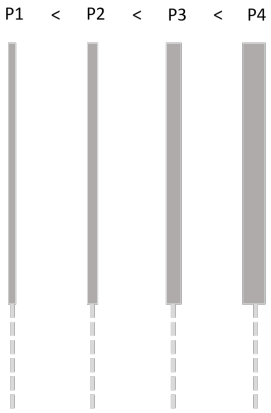

Figure 2.3.4 – Line scanning pattern used for spectra gathering while direct laser writing. Each line was written at different laser powers, and were separated by a minimum distance of 20 μm.

One important aspect to take into consideration when analysing the spectra gathered from the direct laser writing process on (SZ2080+1%IRG)+UCNCs is the fact that *Irgacure 369* photoinitiator also emits fluorescence when excited by the writing laser in a wavelength range that includes the wavelength range of interest for FIR calculations - seen in figure 2.3.5. In order to correct the (SZ2080+1%IRG)+UCNCs spectra without influencing the FIR value, the same line-scanning laser-writing process was executed in a SZ2080+1%IRG sample (undoped with UCNCs) using the same writing power as the one used for processing the

(SZ2080+1%IRG)+UCNCs sample. The gathered photoinitiator fluorescence was then subtracted from the (SZ2080+1%IRG)+UCNCs sample spectra.

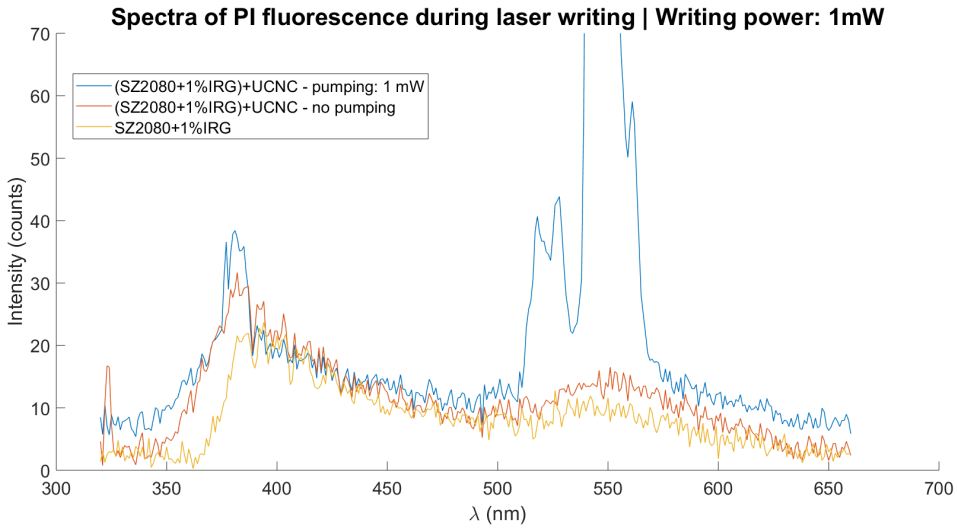

Figure 2.3.5 – Fluorescence spectra of three different samples during direct laser writing to study the influence of *Irgacure 369* photoinitiator fluorescence on the (SZ2080+1%IRG) +UCNCs sample spectra. All spectra were gathered with a writing power of 1 mW.

Chapter 3

Results and Discussion

In this chapter we will be discussing the results on *in-situ* focal volume temperature measurements done on pure and *Irgacure 369* photoinitiator doped SZ2080 photoresist, in order to understand if the different underlying mechanics behind the polymerization of pure and PI doped photoresists have a different, measurable, influence in the voxel temperature during DLW. For this, a temperature calibration was made in order to attribute FIR values, calculated from the fluorescent spectra of the UCNCs to temperature values. This FIR *vs* Temperature fit was then used to measure local temperature values during laser writing, using the calculated FIR from spectra gathered during that process.

3.1 Temperature calibration of UCNCs FIR values

For the temperature calibration, the method described in 2.3.1 was followed for both samples: SZ2080+UCNCs 80:1 [w/w] and (SZ2080+1%IRG)+UCNCs 80:1 [w/w]. The resulted FIR values for different temperature values are depicted in the left plot of figure 3.1.1. The plotted data presents an exponential dependence of FIR values with temperature, as predicted by equation 1.10 in section 1.2.1. The main data points represent the mean FIR value, extracted from the 600 spectra taken for each temperature. The Y-axis error bars in that plot represent the standard deviation of all the FIR values obtained for each temperature.

To explore the exponential dependence of FIR values on temperature, the data of ln(FIR) against the inverse of temperature (T^{-1}) is plotted, as seen on the right-side plot of figure 3.1.1, resulting in a linear distribution of the calibration data. This linear relation between ln(FIR) and T^{-1} is easily seen by rearranging equation 1.10 into the form of equation 3.1. The characteristics of the optical system and its influence in the FIR calculation are also considered in constant C.

$$ln(FIR) = A.T^{-1} + B, \quad \text{for } A = \left(-\frac{\Delta E}{k_B}\right), \; B = ln(C). \tag{3.1}$$

Equation 3.1 can then be fitted to the figure 3.1.1 plotted data for both samples, resulting in the values for coefficients A and B presented in table 3.1. Due to the choice of integration limits explained in section 2.3, the A coefficients of table 3.1, resulting from the fitted data, are not equal to $-\Delta E/k_B$. Since we are only integrating part of the peak, the value we get from multiplying A and $-k_B$ is not ΔE, but a fraction of it. Since the integration values are maintained constant throughout the experiment, the ΔE fraction value will remain constant as well, preserving the linear relation between ln(FIR) and T^{-1}.

From equation 3.1, and using the coefficients given by table 3.1, one can calculate the local temperature using FIR values with the formula:

$$T(FIR) = A.\big(ln(FIR) - B\big)^{-1} \tag{3.2}$$

Table 3.1 – Coefficients A and B resulting from fitting equation 3.1 to the data plotted in figure 3.1.1.

Sample:	**Fitted coeff. values**	
	A	***B***
SZ2080+UCNCs 80:1 [w/w]	-992.4 ± 3.6	2.263 ± 0.05
(SZ2080+1%IRG)+UCNCs 80:1 [w/w]	-980.5 ± 4.3	2.190 ± 0.028

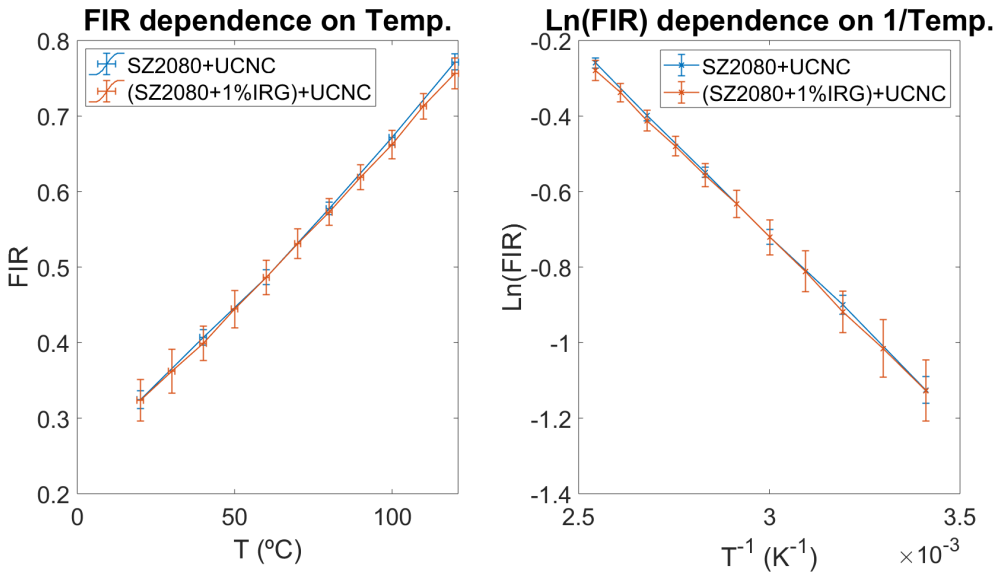

Figure 3.1.1 – Plotted data from temperature calibration.**(Left)** mean FIR values calculated for each temperature, for both samples. Error bars are the standard deviation values. **(Right)** Linearization of the plot on the left, in order to comply with equation 3.1.

3.2 Temperature measurements during laser writing: pure and PI doped SZ2080

Following the procedure presented in section 2.3.2, both SZ2080+UCNCs 80:1 [w/w] and (SZ2080+1%IRG)+UCNCs 80:1 [w/w] samples were subjected to direct laser writing at different laser powers. During the writing process, the fluorescence spectra emitted by the pumped UCNCs on the samples were collected and analysed in order to estimate the voxel local temperature. In order to get temperature values using the FIR from the gathered spectra, equation 3.2 was used, applying the proper A and B coefficients of table 3.1.

For the SZ2080+UCNCs 80:1 [w/w] sample, the writing powers used were 1.25, 1.50, 1.75, 2.00, 2.25 and 2.50 mW. The measured temperatures for each writing power, compared to the temperature measured on the sample before the laser writing started are presented in table 3.2, and are plotted in figure 3.2.1 along with a CMOS image of the written lines.

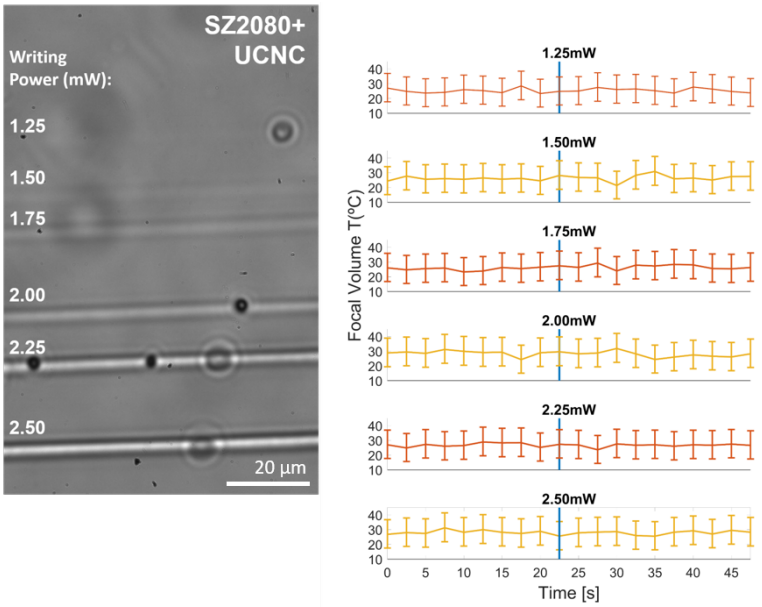

Figure 3.2.1 – **(Left)** CMOS camera image of the scanned lines during direct laser writing with the associated writing powers. **(Right)** Time lapse of focal volume temperature before and during direct laser writing for the SZ2080+UCNCs sample. The blue mark represents the point in time where the writing laser was turned on. Data points are the average value of 10 sequenced FIR values.

Table 3.2 – Focal volume average temperature values measured before and during direct laser writing at different laser writing powers for the PI undoped sample SZ2080+UCNCs.

SZ2080+UCNCs	**Before laser writing**	**During laser writing**
Writing power (mW)	$T_{avg.}$ (^oC)	$T_{avg.}$ (^oC)
1.25	25.13 ± 9.32	25.55 ± 9.42
1.50	26.07 ± 9.26	26.38 ± 9.27
1.75	25.52 ± 9.24	26.92 ± 8.83
2.00	28.95 ± 9.36	27.79 ± 11.71
2.25	26.99 ± 9.29	26.64 ± 9.28
2.50	28.18 ± 9.33	27.69 ± 9.32

For the (SZ2080+1%IRG)+UCNCs 80:1 [w/w] sample, the writing powers used were considerably lower: 0.75, 1.00, 1.25 and 1.50 mW. The same temperature analysis was made, taking into account the needed spectra correction, due to PI fluorescence, presented in section 2.3.2. A table of average focal volume temperature values is presented in 3.3, and a time lapse plot of focal volume temperature is presented in figure 3.2.2.

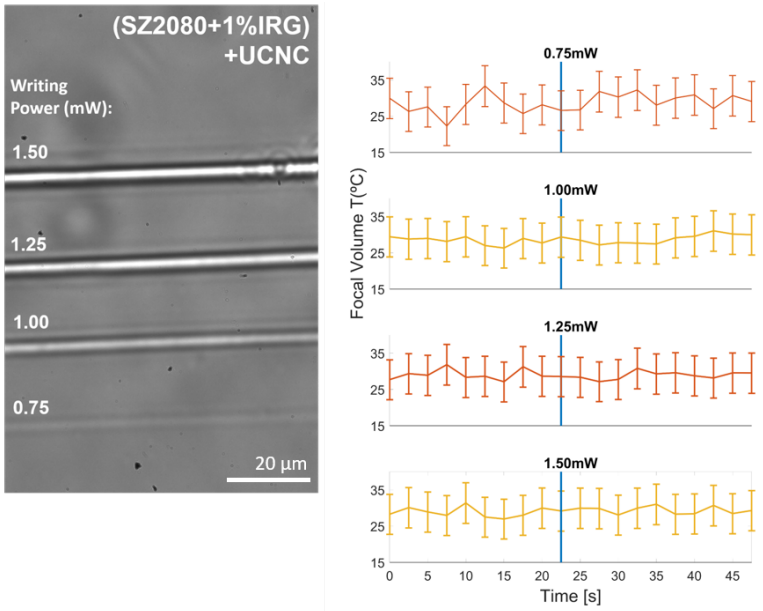

Figure 3.2.2 – **(Left)** CMOS camera image of the scanned lines during direct laser writing with the associated writing powers. **(Right)** Time lapse of focal volume temperature before and during direct laser writing for the (SZ2080+1%IRG)+UCNCs sample. The blue mark represents the point in time where the writing laser was turned on. Data points are an average value of 10 time-sequenced FIR values.

Table 3.3 – Focal volume average temperature values measured before and during direct laser writing at different laser writing powers for the PI doped sample (SZ2080+1%IRG)+ UCNC.

(SZ2080+1%IRG)+UCNCs	**Before laser writing**	**During laser writing**
Writing power (mW)	$T_{avg.}$ (^oC)	$T_{avg.}$ (^oC)
0.75	27.69 ± 5.55	29.41 ± 5.60
1.00	28.42 ± 2.57	28.90 ± 5.58
1.25	29.04 ± 5.59	28.90 ± 5.57
1.50	28.83 ± 5.59	29.38 ± 5.60

3.3 Discussion

The temperature calibration was successful in the way that it demonstrated a high linear profile for the dependence of ln(FIR) values with the inverse temperature (T^{-1}), as seen in the left plot of figure 3.1.1. It was also proven experimentally, even if not explicit in this work, the reproducibility of FIR values for each temperature when using the same sample.

This serves as a demonstration on the viability of using $NaGdF_4$:Er^{3+},Yb^{3+} nanocrystals for temperature sensing applications, even when in a solution of SZ2080 photoresist.

As for the temperature measurements taken for both SZ2080+UCNCs 80:1 [w/w] and (SZ2080+1%IRG)+UCNCs 80:1 [w/w], the results shown on both tables 3.2 and 3.3 present no considerable differences between the *Before laser writing* and the *During laser writing* values. Even though the large uncertainties associated with the temperature values (no less than 8.5ºC), no increase on average temperature was detected during the laser writing processing of both samples, comparing to the initial temperatures before writing.

On the specific case of the SZ2080+UCNCs sample, where focal volume temperature was expected to rise due to avalanche ionization being the only process behind polymerization initiation, the results show no temperature variance larger than 1.40ºC (for 1.75 mW of writing power) between before and during laser writing. These results disagree with the results in [Varapnickas et al., 2018], where the measured temperature during the processing of SZ2080 photoresist, doped with the same $NaGdF_4$:Er^{3+},Yb^{3+} upconverting nanocrystals, showed a ~20ºC temperature increase during laser writing. This discrepancy between our results and the ones on [Varapnickas et al., 2018] can be explained by the fact that we used a lower concentration of UCNCs in our samples (80:1 [w/w] *vs* 43:15 [w/w]), and, as seen in section 2.2, high UCNCs concentration in photoresist might result in micro-explosions that substantially increase the temperature of the sample in the focal volume region.

For the values of focal volume temperature gathered for the (SZ2080+1%IRG)+UCNCs 80:1 [w/w] one gets the same behaviour of no increase in the average temperature. In [Mueller et al., 2013], a 3ºC temperature rise in the focal volume is observed in a sample of (pentaerythritol triacrylate+2%Irgacure 819) during laser writing. This result could hardly be reproduced in this work with such precision, due to the uncertainties relative to the measured temperature values.

The strange phenomena of having higher temperature values before writing than during writing, in some cases, can be explained by two main factors: a non-uniform temperature of

the sample and small variances in the gathered fluorescence shape due to background light interference.

The fact that no relevant temperature increase was observed, contrary to the expected result, might arise from broad spatial filtering, which captures fluorescence not only from the focal volume but also from the surrounding material. The exact volume from which luminescence was gathered is unknown, but the only spatial filtering done was the use of a 200 μm diameter core optical-fibre as a pin-hole, which is ~ 10 times larger than the expected axial dimension of the focal volume. Capturing the fluorescence of the material surrounding the focal volume (and the voxel) decreases the overall average measured temperature. The absence of focal volume temperature variations, plus the random behaviour of temperature values, turns the main results inconclusive, not proving if the temperature of the voxel is in fact greater for pure SZ2080 than for *Irgacure 369* doped SZ2080.

Possible improvements can be done to this set-up to increase success rate on future experiments. Two improvement examples are the use of an optical-fibre with a reduced core diameter, for better spatial filtering, and a continuous-wave laser for UCNC pumping, which enables the use of higher pumping powers without affecting the sample. It is also advised a further study on how to correct the UCNCs fluorescence spectra collected from *Irgacure 369* doped samples.

Chapter 4

Conclusion and future perspectives

In this work we have investigated the local temperature in photoinitiator (PI) doped and undoped SZ2080 photoresist samples during the process of 3D direct laser writing (3D DLW), using upconverting nanocrystals (UCNs) for high spatial resolution sensing of temperature. This was made in order to try to understand the influence of different underlying mechanics of photopolymerization for PI doped and undoped SZ2080 on voxel temperature.

For this, an optical set-up based on [Mueller et al., 2013], combining a 3D DLW system and a fluorescence microscope was developed. This set-up consisted mainly of two laser sources for writing and pumping, a common objective lens for focussing the laser beams and collect the fluorescence emitted by the UCNCs, present in the sample, a CMOS camera for imaging and a spectrograph for fluorescence spectra analysis. This set-up was used to study two main samples of SZ2080 photoresist (pure and doped with *Irgacure 369* photoinitiator), prepared in a ratio of 80:1 [w/w] with $NaGdF_4$: Yb^{3+}, Er^{3+} upconverting nanocrystals (UCNCs). The presence of UCNCs in the sample enabled the temperature sensing through FIR (fluorescence intensity ratio) calculations using their upconversion fluorescence spectra.

The built system was successfully able to calibrate the FIR values, calculated from the captured UCNCs spectra, with the sample temperature, following the theoretically expected exponential dependence of FIR values on temperature. Using this temperature calibration,

we were able to measure the local temperature during direct laser writing.

Upon measuring the local temperature for both SZ2080+UCNCs and (SZ2080+1%IRG)+ UCNCs samples during direct laser writing, no temperature increase was observed, contrary to the results presented in [Varapnickas et al., 2018, Mueller et al., 2013]. The reason for this absence of temperature variation might lay on a broad spatial filtering by the optical system, which results in measuring a large volume surrounding the voxel, averaging the overall temperature of that volume. Further improvements on the set-up can be done, in particular on the spatial filtering and laser pumping.

The optical set-up newly developed in this work proved to be essential to a fine analysis of SZ2080 with a low concentration of UCNCs (unlike that used in [Varapnickas et al., 2018]), highlighting the need of further research for a full comprehension of the mechanisms involved. This work is thus likely to serve as a solid ground for further studies on the particular topic of local thermal effects during 3D DLW, as well as in other topics related to temperature sensing using Yb^{3+}, Er^{3+} doped upconverting nanocrystals.

Bibliography

[Aigouy et al., 2005] Aigouy, L., Tessier, G., Mortier, M., and Charlot, B. (2005). Scanning thermal imaging of microelectronic circuits with a fluorescent nanoprobe. *Applied Physics Letters*, **87**(184105).

[Baziulyte-Paulaviciene et al., 2017] Baziulyte-Paulaviciene, D., Karabanovas, V., Stasys, M., Jarockyte, G., Poderys, V., Sakirzanovas, S., and Rotomskis, R. (2017). Synthesis and functionalization of NaGdF4:Yb,Er@NaGdF4 core–shell nanoparticles for possible application as multimodal contrast agents. *Beilstein J Nanotechnol.*, **8**:1815–1824.

[Burmeister et al., 2012a] Burmeister, F., Steenhusen, S., Houbertz, R., Zeitner, U. D., Nolte, S., and Tünnermann, A. (2012a). Materials and technologies for fabrication of three-dimensional microstructures with sub-100 nm feature sizes by two-photon polymerization. *Journal of Laser Applications*, **24**(042014).

[Burmeister et al., 2012b] Burmeister, F., Zeitner, U. D., Nolte, S., and Tünnermann, A. (2012b). High numerical aperture hybrid optics for two-photon polymerization. *Optics Express*, **20**(7).

[Cao et al., 2015] Cao, B. S., Wu, J., Wang, X. H., He, Y. Y., Feng, Z. Q., Dong, B., and Rino, L. (2015). Multiple temperature effects on up-conversion fluorescences of Er3+ -Yb3+ -Mo6+ codoped TiO2 and high thermal sensitivity. *AIP Advances*, **5**(087136).

[Danilevičius et al., 2013] Danilevičius, P., Rekštyt, S., Balčiunas, E., Kraniauskas, A., Sirmenis, R., Baltriukien, D., Bukelskienand, V., Gadonas, R., Sirvydis, V., Piskarskas, A., and Ma-

linauskas, M. (2013). Laser 3D micro/nanofabrication of polymers for tissue engineering applications. *Optics & Laser Technology*, **45**:518–524.

[de Araújo et al., 2009] de Araújo, M. A. C., Silva, R., Lima, E., and de Oliveira, P. C. (2009). Measurement of Gaussian laser beam radius using the knife-edge technique: Improvement on data analysis. *Applied Optics*, **48**(2).

[Fischer et al., 2013] Fischer, J., Mueller, J. B., Kaschke, J., Wolf, T. J. A., Unterreiner, A.-N., , and Wegener, M. (2013). Three-dimensional multi-photon direct laser writing with variable repetition rate. *OPTICS EXPRESS*, 21(**22**).

[Fuchs et al., 2006] Fuchs, U., Zeitner, U. D., and Tünnermann, A. (2006). Hybrid optics for focusing ultrashort laser pulses. *Optics Express*, **31**(10).

[Jaque and Vetrone, 2012] Jaque, D. and Vetrone, F. (2012). Luminescence nanothermometry. *Nanoscale*, **4**(4301).

[Jiang et al., 2014] Jiang, L. J., Baldacchini, T., Zhou, Y. S., Xiong, W., Gao, Y., Huang, X., Jiang, L., Silvain, J.-F., and Lu, Y. F. (2014). Two-photon polymerization: investigation of chemical and mechanical properties of resins using Raman microspectroscopy. *Optics Letters*, **39**(10).

[Jonušauskas et al., 2017] Jonušauskas, L., Gailevičius, D., Mikoliūnaitė, L., Sakalauskas, D., Šakirzanovas, S., Juodkazis, S., and Malinauskas, M. (2017). Optically Clear and Resilient Free-Form micro-Optics 3D-Printed via Ultrafast Laser Lithography. *Materials*, **10**(1).

[Kawata et al., 2001] Kawata, S., Sun, H.-B., Tanaka, T., and Takada, K. (2001). Finer features for functional microdevices. *Nature*, **412**:697–698.

[Mack, 2007] Mack, C. (2007). *Fundamental Principles of Optical Lithography: The Science of Microfabrication*. Wiley.

[Malinauskas et al., 2013] Malinauskas, M., Farsari, M., Piskarkas, A., and Juodkazis., S. (2013). Ultrafast laser nanostructuring of photopolymers: A decade of advances. *Physics Report*, **533**:1–31.

[Malinauskas et al., 2010] Malinauskas, M., Žukauskas, A., Bičkauskaitė, G., Gadonas, R., and Juodkazis, S. (2010). Mechanisms of three-dimensional structuring of photopolymers by tightly focussed femtosecond laser pulses. *Optics Express*, **18**(10).

[Malinauskas et al., 2016] Malinauskas, M., Žukauskas, A., Bičkauskaitė, G., Hasegawa, S., Hayasaki, Y., Mizeikis, V., Buividas, R., and Juodkazis, S. (2016). Ultrafast laser processing of materials: from science to industry. *Light: Science & Applications*, **5**.

[Mueller et al., 2013] Mueller, J. B., Fischer, J., Mange, Y. J., Nann, T., and Wegeners, M. (2013). In-situ local temperature measurement during three-dimensional direct laser writing. *Appl. Phys. Lett.*, **103**(123107).

[Ovsianikov et al., 2008] Ovsianikov, A., Viertl, J., Chichkov, B., Oubaha, M., MacCraith, B., Sakellari, I., Giakoumaki, A., Gray, D., Vamvakaki, M., Farsari, M., and Fotakis, C. (2008). Ultra-low shrinkage hybrid photosensitive material for two-photon polymerization microfabrication. *ACS Nano*, **2**(11).

[Schafer et al., 2004] Schafer, K. J., Hales, J. M., Balu, M., Belfield, K. D., Stryland, E. W. V., and Hagan, D. J. (2004). Two-photon absorption cross-sections of common photoinitiators. *Journal of Photochemistry and Photobiology A: Chemistry*, **162**:497–502.

[Sun and Kawata, 2004] Sun, H.-B. and Kawata, S. (2004). Two-Photon Photopolymerization and 3D Lithographic Microfabrication. *Adv Polym Sci*, **170**:169–273.

[Žukauskas et al., 2016] Žukauskas, A., Malinauskas, M., Brasselet, E., and Juodkazis, S. (2016). *3D Micro-Optics Via Ultrafast Laser Writing: Miniaturization, Integration, and Multifunctionalities*, chapter **12.1**. Elsevier.

[Žukauskas et al., 2015] Žukauskas, A., Matulaitienė, I., Paipulas, D., Niaura, G., Malinauskas, M., and Gadonas, R. (2015). Tuning the refractive index in 3D direct laser writing lithography: towards GRIN microoptics. *Laser Photonics Rev.*, **9**(6):706–712.

[Varapnickas et al., 2018] Varapnickas, S., Baziulytė-Paulavičienė, D., Šakirzanovas, S., and Malinauskas, M. (2018). Local temperature measurement during ultrafast laser 3D nanolithography writing. In *Proceedings of SPIE*.

[Vetrone et al., 2010] Vetrone, F., Naccache, R., Zamarrón, A., de la Fuente, A. J., Sanz-Rodríguez, F., Maestro, L. M., Rodriguez, E. M., Jaque, D., Solé, J. G., and Capobianco, J. A. (2010). Temperature Sensing Using Fluorescent Nanothermometers. *ACS NANO*, **4**:3254–3258.

[Xu et al., 1998] Xu, Y. Z., Tam, H. Y., Liu, S. Y., and Demokan, M. S. (1998). Pump-Induced Thermal Effects in Er–Yb Fiber Grating DBR Lasers. *IEEE Photonics Technology Letters*, **10**(9).

[Zhan, 2016] Zhan, Q. (2016). *Focusing Trough High-Numerical Aperture Objective*, chapter 7. Elsevier.

Appendices

Appendix A

Spectra shape dependence on Pumping power and UCNC weight ratio

[Image in the next page]

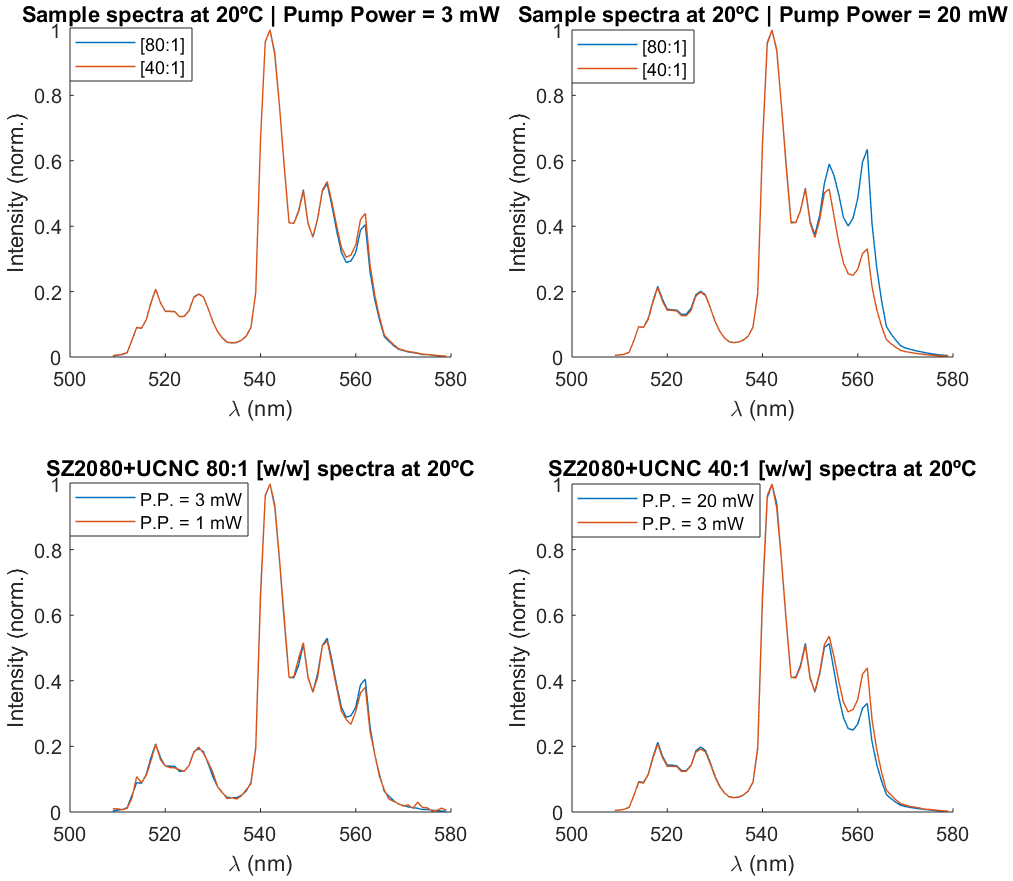

Figure A.0.1 – Sample spectra shape dependence on different experimental conditions. All spectras are normalized to their highest peak value. **(Top plots)** Shape dependence on UCNC weight ratio on the sample. **(Bottom plots)** Shape dependence on laser pumping power.